frontiers | Frontiers in Earth Science

TYPE Original Research
PUBLISHED 06 January 2023
DOI 10.3389/feart.2022.1000603

OPEN ACCESS

EDITED BY
Fan Yang,
Lanzhou University, China

REVIEWED BY
Zesheng Qian,
Lanzhou University, China
Peng-Peng Yu,
Sun Yat-sen University, China
Liang Liu,
Institute of Geochemistry, Chinese Academy of Sciences (CAS), China

*CORRESPONDENCE
He Li,
lihe@qdio.ac.cn

SPECIALTY SECTION
This article was submitted to Geochemistry, a section of the journal Frontiers in Earth Science

RECEIVED 22 July 2022
ACCEPTED 20 September 2022
PUBLISHED 06 January 2023

CITATION
Li J, Li H, Li C, Song M, Jiang M, Yuan S and Zhang L (2023), Early cretaceous ridge subduction in the Shandong Peninsula, Eastern China, indicated by Laoshan A-type granite.
Front. Earth Sci. 10:1000603.
doi: 10.3389/feart.2022.1000603

Early cretaceous ridge subduction in the Shandong Peninsula, Eastern China, indicated by Laoshan A-type granite

Jie Li[1,2], He Li[2,3]*, Congying Li[2,3], Mingchun Song[1,4], Mengyao Jiang[1], Shuai Yuan[2,3] and Lipeng Zhang[2,3]

[1]Hebei Key Laboratory of Strategic Critical Mineral Resources, Hebei GEO University, Shijiazhuang, China, [2]Institute of Oceanology, Chinese Academy of Sciences, Qingdao, China, [3]Laoshan Laboratory, Qingdao, China, [4]Shandong Provincial No 6 Exploration Institute of Geology and Mineral Resources, Weihai, China

Early Cretaceous A-type granites are widespread in the Shandong Peninsula, which can be used to elucidate the tectonic evolution of the eastern China and the destruction of the North China Craton. However, their genesis is still controversial. Several competing models, ranging from slab break-off, postorogenic extension, foundering of the lower crust and ridge subduction, were proposed. Here, we report zircon U–Pb ages, whole-rock and apatite geochemical compositions of the Laoshan granite and discuss its tectonic implications. The Laoshan granite has typical characteristics of A-type granite with high $FeO^T/(FeO^T + MgO)$ ratios (0.90–0.97) and 10000*Ga/Al ratios (2.70–3.36) and high total alkali ($Na_2O + K_2O$: 7.95–8.70 wt%) contents and Zr+Nb+Ce+Y (most >350 ppm) concentrations. The Laoshan granite is further classified as A_1-type based on the Yb/Ta-Y/Nb and Ce/Nb-Y/Nb diagrams and the Nb-Y-3Ga and Nb-Y-Ce triangular discriminant diagrams. Zircon U–Pb dating of two Laoshan granite samples yielded emplacement ages of 117.8 ± 1.0 Ma and 120.1 ± 1.3 Ma, respectively. The oxygen fugacity of the Laoshan granite magma is low, as indicated by zircon Ce^{4+}/Ce^{3+} ratios (most <300). The crystallization temperature of zircon varies significantly, ranging from 652 to 830°C. The apatite compositions show that the Laoshan granite has high F (2.09–2.72 wt%) and low Cl (0.01–0.09 wt%) contents, consistent with influence by fluid released from the decomposition of phengite. Apatite rare earth elements show that mantle sources are also involved in Laoshan A-type granite. Combined previous studies of A-type granitic plutons in the Shandong Province and the Lower Yangtze River belt with the drifting history of the Pacific plate, we propose that the flat subduction of the spreading ridge between the Pacific and the Izanagi plates was responsible for the formation of Laoshan A-type granite.

KEYWORDS

ridge subduction, apatite, zircon U-Pb age, Laoshan A-type granite, Shandong peninsula

Introduction

The North China Craton (NCC) is one of the oldest and most stable cratons in the world. In the Paleozoic, the lithospheric thickness of the NCC reached 200 km. However, after the Mesozoic, the lithospheric thickness in the eastern NCC decreased to about 80 km (Fan and Menzies, 1992; Xu, 2001), accompanied by a series of Yanshanian (Early Cretaceous) tectonic movements and magmatic activities (Wu et al., 2005), which produced a large amount of granitic magma, mainly concentrated ca. 160 ~ 110 Ma (Li et al., 2014; Song et al., 2015, 2017, 2019). The genesis and tectonic background of these granites have been controversial, mainly including slab break-off, slab rollback, postorogenic extension, foundering of the lower lithosphere (Yang et al., 2005, 2018a, 2020a; Liu et al., 2008, 2013; Xie et al., 2009; Goss et al., 2010) and flat ridge subduction (Li et al., 2012a, 2014; Ling et al., 2013), which limit the in-depth understanding of the regional tectonic background.

A-type granite is a special rock formed in an extensional environment, which refers to non-orogenic and water-poor alkaline granite (Loiselle and wones, 1979). According to the tectonic setting, it can be formed not only in the extensional environment within the plate but also in the extensional environment of the plate margin after the collision (Whalen et al., 1987; Eby, 1990, 1992; Bonin, 2007). Eby (1992) classified A-type granites into A1-type and A2-type granites according to their element ratios. A-type granites have unique geochemical characteristics and specific formation conditions and especially have important indicative significance for the tectonic environment. Therefore, the study of Mesozoic A-type granites has important geological significance for Yanshanian tectonic activity in eastern China.

There is an NEE-trending A-type granite belt developed along the Shandong Peninsula, mainly distributed in Wulian, Jiaonan, Laoshan, Haiyang and other places (Wang et al., 1995; Li et al., 2014; Yuan et al., 2022), which provides a good object for us to study the Mesozoic tectonic background and crustal evolution. In this study, we conduct whole-rock geochemistry, zircon U–Pb dating and trace element and apatite trace element composition studies of the Laoshan A-type granite and compare it with A-type granites in the Lower Yangtze River (LYR) belt and Haiyang A_1-A_2-type granite in the Shandong Peninsula, aiming at understanding the genesis of the Early Cretaceous A-type granite in the Shandong Peninsula and discussing the dynamic mechanism of the NCC.

Geological background

The Shandong Peninsula is located at the southeastern margin of the NCC and the eastern part of the Dabie-Sulu orogenic belt (Sun et al., 2002a). The eastern extension of the Qinling-Dabie-Sulu orogenic belt cuts across the southern Peninsula (Li et al., 1993; Goss et al., 2010). It is famous for a large number of gold deposits (Zhai et al., 2002; Deng et al., 2015, 2020; Song et al., 2015, 2021; Fan et al., 2016; Zhang et al., 2017a, 2020a, 2020b; Groves et al., 2020; Li et al., 2020, 2021) with a total controlled Au reserve of more than 5,000 tons (Song et al., 2021). The famous Tan-Lu fault zone separates the Shandong Peninsula into the Luxi and Jiaodong segments (Li et al., 1993; Goss et al., 2010; Tan et al., 2012).

The tectonic units of the Jiaodong segment include the Jiaobei uplift, the Jiaolai basin, and the Weihai uplift. Multistage Mesozoic plutons emplaced within the Precambrian geological units occur in the Jiaobei uplift and the Weihai uplift, including Jurassic granites (the Linglong-type granite, the Wendeng-type granite and the Duogushan-type granite) and Cretaceous granites (the Guojialing-type granodiorite, the Weideshan-type granite and the Laoshan-type granite) (Song et al., 2015, 2017, 2019).

There is an NEE-trending A-type granite belt of approximately 500 km in length across the whole Shandong Peninsula (Wang et al., 1995, 2009). The epochs of the Cretaceous A-type granites range between 110 Ma and 123 Ma (Zhao et al., 1997; Goss et al., 2010; Liu et al., 2013; Li et al., 2014; Yan and Shi, 2014; Gao et al., 2019; Yuan et al., 2022).

The Laoshan granite is located in eastern Qingdao city with a total outcrop area of ~600 km^2. It is a part of the Early Cretaceous A-type granite belt in the Shandong Peninsula (Wang et al., 1995, 2009), which intruded into the Proterozoic basement metamorphic rocks of the Jiaonan Group and the Cretaceous sandstone of the Laiyang Group (Figure 1B). The Laoshan granites contain monzogranite, syenogranite, alkali feldspar granite and quartz syenite. We collected monzogranite samples from the western parts of the Laoshan granitic pluton and were composed of medium-to coarse-grained monzogranite. The coordinates of sample LS-40 are 120°26.98′E, 36°14.71′N, and 120°35.03′, 36°8.10′ for LS-41 (Figure 2A). They are slightly fleshy red with massive structures and developed joints (Figures 2B,C). The main minerals include potassium feldspar, quartz, plagioclase, biotite and hornblende (Figures 2D,E). The accessory minerals include zircon and apatite.

Analytical methods

The whole-rock major element contents were analyzed using X-ray fluorescence spectrometry at the State Key Laboratory of Isotope Geochemistry, Guangzhou Institute of Geochemistry, Chinese Academy of Sciences (GIGCAS), and zircon U–Pb dating and trace elements, whole-rock trace elements and apatite trace elements were analyzed using LA-ICPMS at the Key Laboratory of Mineralogy and Metallogeny, GIGCAS. The major elements (including Cl and F) of apatite were analyzed using a JXA-8100 electron microprobe at the State Key

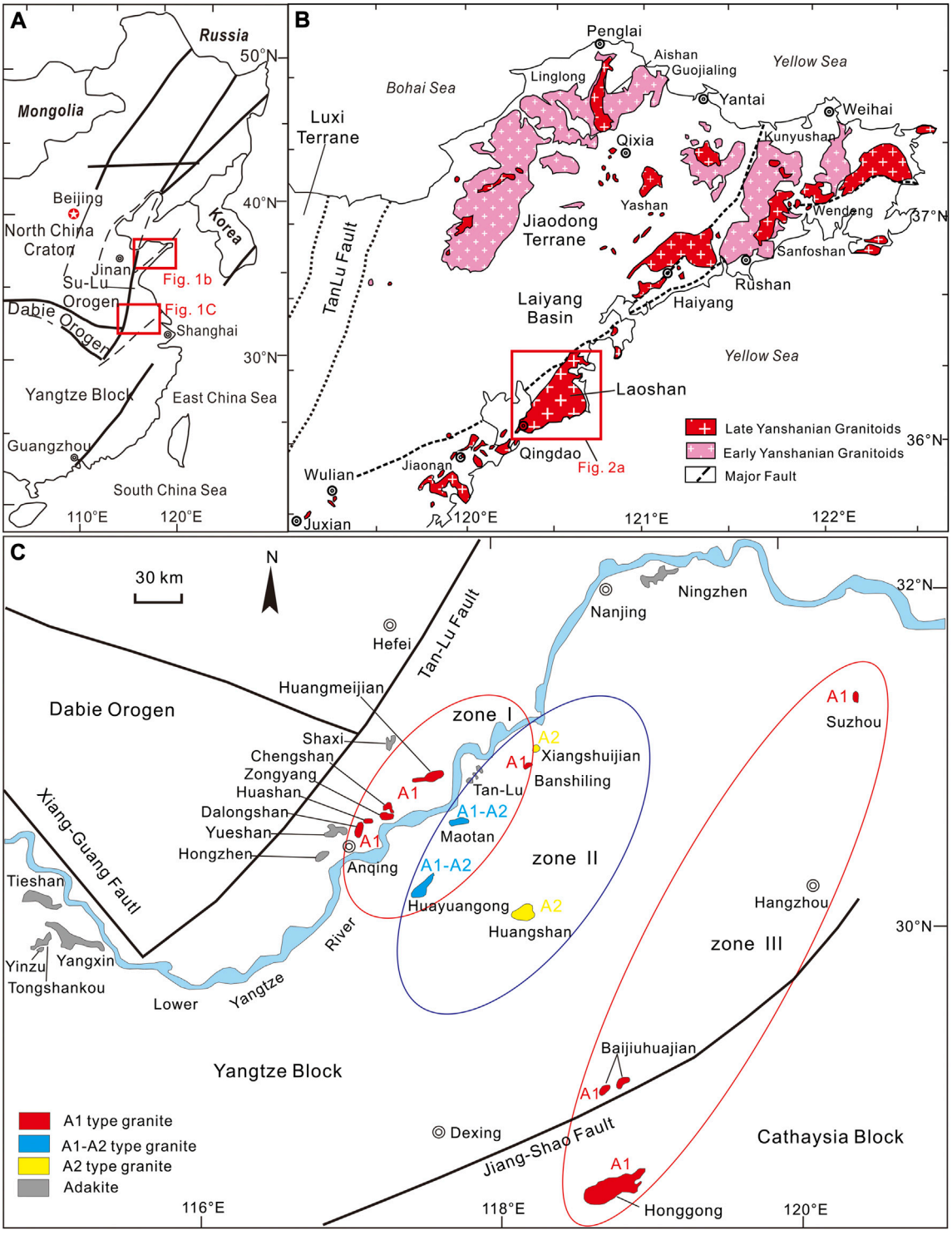

FIGURE 1
(A), Sketch map of the late Mesozoic A-type granites in eastern China. **(B)**, Geological map of the Shandong Peninsula, showing the distribution of Early Yanshanian and Late Yanshanian granitoids of the Jiaodong Terrane (modified after Li et al., 2014). **(C),** Geological map of the Lower Yangtze River (LYR) belt (modified after Li et al., 2012a and related references).

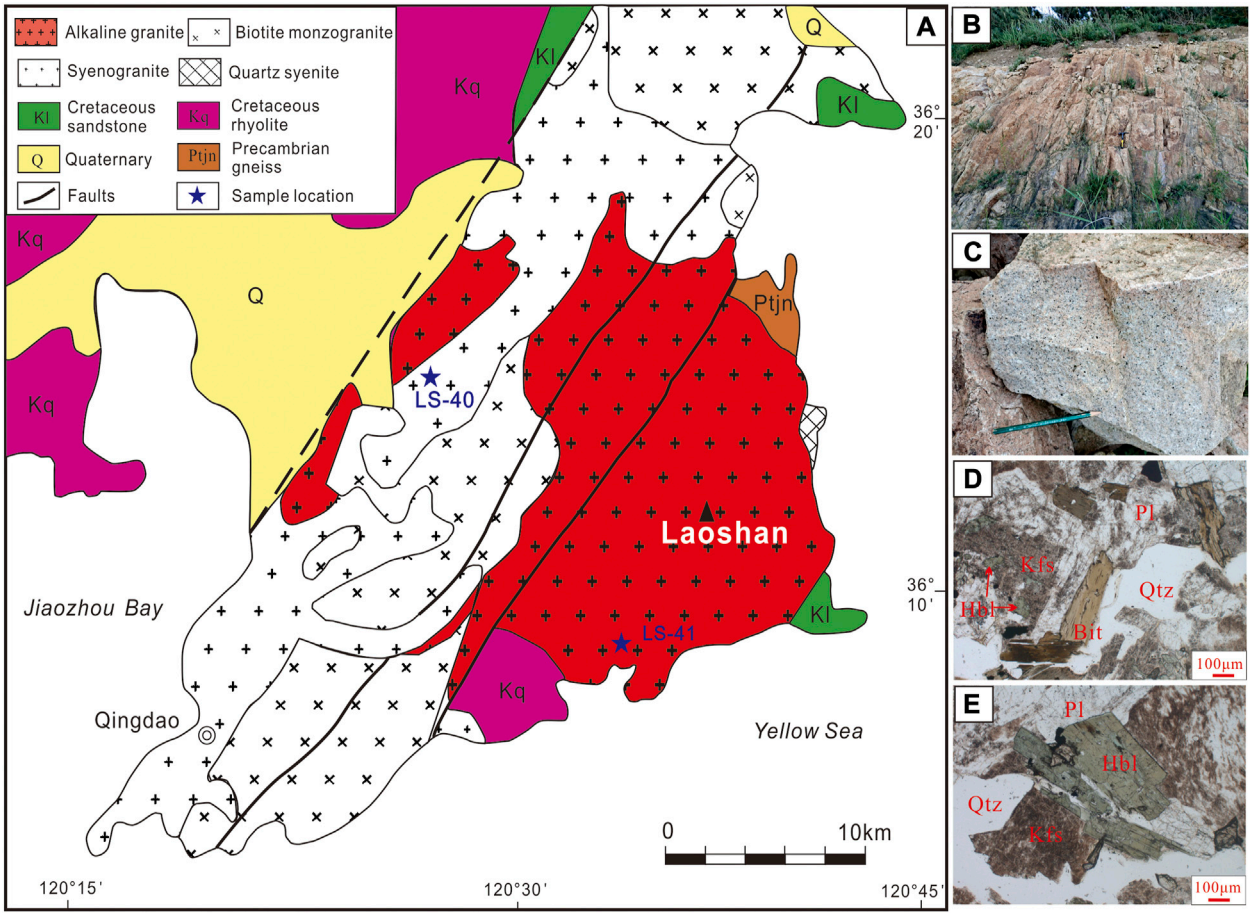

FIGURE 2
(A), Simplified geologic map of the Laoshan granitic complex (modified after Zhao et al., 1997). Field photographs showing **(B,C)** monzogranite of the Laoshan pluton and microphotographs showing **(D,E)** the coarse-grained K-feldspar (Kfs), quartz (Qtz), plagioclase (Pl), biotite (Bit) and hornblende (Hbl) of monzogranite.

Laboratory of Mineral Deposits Research, Nanjing University. The calculations of zircon isotope ratios, the apatite, zircon and whole-rock trace element concentrations were performed using ICPMSDataCal 7.0 (Liu et al., 2010; Lin et al., 2016).

Whole-rock major and trace element analyses

The whole-rock major and trace element contents were analyzed at the State Key Laboratory of Isotope Geochemistry, GIGCAS. The whole-rock major elements were analyzed using X-ray fluorescence spectrometry. The typical analytical precisions were better than 1% (Li et al., 2005). Whole-rock trace element analyses were carried out on fused glasses using LA-ICPMS. The analytical method has been described in more detail by previous authors (Liang et al., 2009; Tu et al., 2011; Li et al., 2012a, Li et al., 2012b). The whole-rock trace element data were calculated using ICPMSDataCal 7.0 (Liu et al., 2010; Lin et al., 2016).

Zircon U–Pb dating and trace element analyses

Zircon grains were obtained through conventional procedures. First, whole rock samples were crushed to about 60 mesh, desliming in water, followed by density separation, magnetic separation and handpicking. Zircon grains were then mounted in epoxy and polished down to nearly half sections to expose internal structures. Cathodoluminescent and optical microscopy images were taken to ensure that the least fractured, inclusion-free parts were analyzed. Zircon U–Pb dating and trace element analyses were carried out at the Key Laboratory of Mineralogy and Metallogeny, GIGCAS. LA-ICPMS was performed following the same technique as that

used for whole-rock analyses (Li et al., 2012a; Li et al., 2012b). The calculations of zircon isotope ratios and zircon trace element concentrations were performed using ICPMSDataCal 7.0 (Liu et al., 2010; Lin et al., 2016). Zircon Ce anomalies were calculated using software from the Research School of Earth Sciences, Australian National University (Ballard et al., 2002; Liang et al., 2006), and the zircon age was calculated using Isoplot (Version 3.23).

Apatite major and trace element analyses

Fluorine and chlorine compositions of apatite were determined using a JXA-8100 electron microprobe at the State Key Laboratory of Mineral Deposits Research, Nanjing University. The analysis conditions were 15 keV and 10 nA current, with a 10 μm diameter electron beam. A norbergite grain was used as a standard for F, $Ba_5(PO_4)_3Cl$ for Cl, and apatite for Ca and P standards. The detailed method was described previously (Li et al., 2012b). The apatite trace elements were analyzed using LA-ICPMS at the Key Laboratory of Mineralogy and Metallogeny, GIGCAS. The conditions were 80 mJ laser energy, with a repetition rate of 6 Hz, a spot size of 41 μm in diameter and a 40 s ablation time. NIST 612 was used as an external standard, NIST 610 was used as a monitoring standard, and ^{43}Ca was used as an internal standard (Liang et al., 2009; Tu et al., 2011; Li H. et al., 2012a, Li et al., 2012b). The calculations of the apatite trace element concentrations were performed using ICPMSDataCal 7.0 (Liu et al., 2008; Lin et al., 2016).

Results

Whole-rock major and trace elements

Major and trace element results of the Laoshan granite samples (*N*=23) are summarized in Table 1. These granite samples have high SiO_2 (76.0–78.2 wt%), K_2O (4.23–4.79 wt%), and Na_2O (3.38–4.09 wt%) contents and low Al_2O_3 (12.3–13.3 wt%), TiO_2 (0.09–0.19 wt%), MgO (0.03–0.10 wt%), $Fe_2O_3^T$ (0.73–1.21 wt%), CaO (0.04–0.33 wt%) and P_2O_5 (0–0.01 wt%) contents. In Harker diagrams, CaO, MgO, Al_2O_3, TiO_2, $Fe_2O_3^T$, and P_2O_5 contents of the Laoshan granite, together with syenogranite and alkali feldspar granite from previous studies (Zhao et al., 1997; Goss et al., 2010; Yan and Shi, 2014), are negatively correlated with SiO_2, whereas no obvious correlation exists between Na_2O, K_2O and SiO_2. The whole-rock Ti thermometer gave a formation temperature of approximately 652–830°C for the monzogranite (Schiller and Finger, 2019; Yu et al., 2022) (Figure 3). The K_2O/Na_2O ratios (1.08–1.39) and $FeO^T/(FeO^T + MgO)$ ratios (0.90–0.97) are lower than those of the Haiyang syenite (0.76–0.87, 1.28–1.58). They are peraluminous with A/CNK ratios from 1.06 to 1.20 and are alkaline rocks with total alkali contents ($K_2O + Na_2O$) ranging from 7.95 to 8.70 wt%.

The Laoshan granite is characterized by high field strength elements, such as Th, U, Zr, and Hf, and high concentrations of large iron lithophile elements, such as K, Rb, Ba, and Na (Table 1; Figure 4A). The samples are depleted in HREEs and enriched in LREEs with $(La/Yb)_N$ from 4.62 to 12.03 and with strong negative Eu anomalies (Figure 4B).

Zircon U–Pb ages

Zircon grains from monzogranite samples LS-40 and LS-41 are mostly prismatic, transparent, pale yellow in color, and approximately 200 μm in size. All zircon grains show clear zonation, as revealed in CL images, which is consistent with typical igneous zircons. Inherited cores are rare and, if there are any, surrounded by prismatic and transparent rims. The zircon U–Pb isotope compositions are shown in Table 2 and are also shown in the concordia diagram (Figure 5).

\Twenty-two available zircon data points for sample LS-4002 were obtained. The zircon Th and U concentrations range from 104 to 2,845 ppm and from 182 to 1,146 ppm, respectively (Table 2), corresponding to Th/U ratios from 0.43 to 2.48. Eighteen zircon grains from sample LS-4109 were analyzed. The zircon Th concentrations range from 295 to 3,678 ppm, and the U concentrations range from 182 to 1,298 ppm (Table 2), with Th/U ratios ranging from 1.37 to 3.63. These Th/U ratios are typical magmatic geneses (Hoskin and Black, 2000; Belousova et al., 2002; Sun et al. 2002b). Samples LS-4002 and LS-4109 yield a weighted mean $^{206}Pb/^{238}U$ age of 117.8 ± 1.0 Ma and 120.1 ± 1.3 Ma, respectively (Figure 5; Table 2), which represent crystallization ages of 117.8 ± 1.0 Ma to 120.1 ± 1.3 Ma for the monzogranite.

Zircon trace elements

The zircon trace element concentrations are shown in Table 3. The negative Eu and positive Ce anomalies are shown in the chondrite-normalized REE diagram. The zircon Ce^{4+}/Ce^{3+} ratios of sample LS-4002 range from 8 to 181, indicating relatively low oxygen fugacities. The zircon Ce^{4+}/Ce^{3+} ratios of sample LS-4109 have relatively higher variations (from 1 to 380, except one of 505) than those from LS-4002, but most of them have low oxygen fugacities (Ballard et al., 2002; Liang et al., 2006). The crystallization temperature of zircon ranges from 652 to 830°C according to zircon Ti concentrations (Schiller and Finger, 2019; Yu et al., 2022) (Table 2). These temperatures are comparable to the temperatures of A_2-type granites in the LYR Belt, which range from 650 to 800°C (Li et al., 2012a), and are marginally higher than those of the Haiyang syenite, which ranges from 620 to 780 °C (Li et al., 2014).

TABLE 1 Major and trace element compositions of Laoshan granite.

Sample	LS-4001	LS-4002	LS-4003	LS-4004	LS-4005	LS-4006	LS-4007	LS-4008	LS-4009	LS-4101	LS-4102	LS-4103	LS-4104	LS-4105	LS-4106	LS-4107	LS-4108	LS-4109	LS-4110	LS-4111	LS-4112	LS-4113	LS-4114
SiO_2	76.7	76.0	76.9	76.8	76.8	77.2	76.4	76.6	76.5	76.9	77.5	77.4	76.6	76.8	77.4	76.8	76.4	77.0	77.6	76.6	78.0	76.4	78.2
TiO_2	0.10	0.10	0.11	0.10	0.10	0.09	0.11	0.10	0.10	0.10	0.12	0.11	0.11	0.10	0.12	0.11	0.16	0.19	0.11	0.19	0.11	0.11	0.10
Al_2O_3	13.2	13.3	12.8	13.1	13.0	12.9	13.3	13.1	12.8	12.7	12.3	12.8	13.2	13.1	12.7	13.2	13.2	12.7	12.6	12.6	12.5	13.3	12.5
Fe_2O_3	0.99	1.12	1.10	1.04	1.08	0.90	1.02	1.02	0.91	0.76	0.75	0.85	0.92	0.94	1.07	0.96	1.21	1.18	0.89	0.92	0.81	0.96	0.73
MnO	0.02	0.11	0.04	0.03	0.03	0.03	0.02	0.02	0.05	0.01	0.01	0.01	0.00	0.00	0.01	0.02	0.01	0.01	0.01	0.01	0.01	0.02	0.01
MgO	0.08	0.08	0.08	0.10	0.08	0.06	0.06	0.07	0.06	0.06	0.03	0.04	0.03	0.03	0.04	0.03	0.04	0.03	0.03	0.05	0.03	0.05	0.04
CaO	0.30	0.33	0.33	0.22	0.25	0.25	0.25	0.28	0.32	0.27	0.19	0.13	0.19	0.19	0.10	0.18	0.21	0.2	0.13	0.22	0.16	0.07	0.04
Na_2O	3.48	3.77	3.41	3.37	3.38	3.41	3.56	3.61	3.75	3.45	3.95	3.96	4.01	3.97	3.87	3.91	4.03	3.89	3.85	3.97	3.86	4.09	3.75
K_2O	4.60	4.59	4.61	4.57	4.66	4.72	4.76	4.60	4.53	4.79	4.26	4.38	4.54	4.43	4.29	4.44	4.41	4.40	4.34	4.59	4.23	4.60	4.32
P_2O_5	0.01	0.01	0.01	0.01	0.01	0.01	0.01	0.01	0.00	0.00	0.00	0.01	0.01	0.01	0.01	0.01	0.01	0.01	0.01	0.00	0.01	0.01	0.01
L.O.I	0.50	0.51	0.51	0.61	0.54	0.34	0.44	0.47	0.43	0.37	0.24	0.20	0.24	0.35	0.29	0.26	0.30	0.30	0.30	0.30	0.23	0.25	0.26
Total	99.9	99.9	99.9	99.9	99.9	99.9	99.9	99.9	99.4	99.4	99.4	99.9	99.9	99.9	99.9	99.9	99.9	99.9	99.9	99.4	99.9	99.9	99.9
Sc	1.15	0.98	1.24	1.05	1.39	1.56	0.82	0.97	1.45	0.98	1.53	1.72	3.13	1.89	1.91	2.25	2.00	2.55	1.28	2.23	1.75	1.62	1.00
Ti	578	595	657	605	607	527	637	586	624	605	729	633	646	602	726	660	935	1,112	671	1,147	655	661	575
V	6.29	6.39	6.71	6.44	5.95	6.44	6.67	6.63	6.41	7.81	6.37	6.64	7.17	7.35	6.68	6.88	7.01	8.26	6.65	8.81	7.28	8.12	6.86
Cr	4.31	2.75	1.36	10.14	5.54	4.32	4.46	5.93	2.89	18.1	32.2	5.83	19.1	5.61	8.17	8.57	9.03	5.73	14.0	25.4	3.91	14.6	23.95
Mn	145	815	314	230	213	232	183	176	415	98.0	65.0	47.0	23.0	31.0	109	123	62.0	70.0	94.0	74.0	63.0	125	46.0
Co	0.93	1.22	1.15	2.12	1.71	1.91	1.53	1.17	0.91	0.49	0.72	0.78	0.98	0.81	0.71	1.02	0.49	0.79	0.82	0.88	0.87	0.84	1.30
Ni	4.47	5.94	6.95	2.56	5.47	2.78	4.11	2.56	3.98	18.0	11.2	9.05	20.2	16.2	8.61	7.38	22.7	6.03	22.4	10.6	16.4	8.89	10.5
Zn	49.3	58.3	53.9	48.3	54.3	59.3	38.9	53.0	66.5	83.7	43.5	39.6	50.5	53.9	60.6	67.0	72.7	50.8	58.2	58.9	58.5	58.2	51.0
Ga	19.5	20.3	18.9	18.7	20.3	20.6	19.6	19.6	19.2	20.8	18.9	19.6	20.3	22.3	22.6	23.3	20.8	20.6	21.4	21.9	22.6	19.7	20.3
Rb	196	210	185	147	117	169	155	216	196	182	183	147	163	179	180	171	173	167	176	170	185	137	176
Sr	14.7	15.7	16.4	16.2	16.7	15.7	15.3	13.7	11.4	7.19	14.0	6.73	7.03	8.07	7.81	7.03	7.57	6.17	7.67	7.46	6.92	7.54	5.09
Y	25.7	28.8	28.1	27.1	30.5	30.7	29.1	25.6	31.3	26.6	18.4	20.3	17.0	21.5	20.8	20.9	27.8	35.1	24.7	37.5	24.1	23.2	13.8
Zr	155	156	144	162	192	176	131	154	190	207	117	187	226	239	223	335	240	300	248	281	314	180	141
Nb	54.7	58.2	56.3	48.8	57.5	55.5	44.2	53.2	56.7	36.0	48.4	27.9	30.2	34.5	32.0	38.0	36.5	34.2	35.1	43.9	49.0	27.9	27.0
Ba	64.1	49.6	76.1	65.6	65.5	77.7	65.8	58.5	39.9	28.3	54.6	30.6	28.5	31.1	32.2	35.8	29.7	28.7	29.4	32.2	34.3	26.1	27.5
La	44.0	39.5	49.1	43.6	47.7	43.1	34.9	44.6	46.1	33.6	38.8	26.5	25.7	36.1	33.8	33.6	28.6	45.4	34.7	46.6	40.1	26.2	21.6
Ce	67.9	72.8	86.9	55.8	72.8	82.6	61.6	72.1	75.6	50.1	52.3	43.9	38.7	48.3	45.2	46.0	38.7	62.2	44.7	63.2	56.3	41.2	32.9
Pr	7.76	7.36	8.49	7.89	8.48	7.89	6.48	8.09	8.40	5.04	6.58	3.89	3.72	4.57	4.23	4.41	4.26	7.12	4.71	7.13	5.07	4.30	3.32
Nd	26.9	26.1	32.5	27.8	30.6	28.6	23.3	29.0	30.2	15.2	24.8	12.8	11.5	14.1	14.1	14.8	14.3	25.4	16.8	24.4	16.1	12.9	10.7
Sm	5.04	5.30	6.65	5.56	6.58	5.74	4.73	5.16	6.16	2.55	4.92	1.95	1.89	2.63	2.45	2.58	2.48	4.99	2.74	4.47	2.64	2.03	1.70
Eu	0.15	0.17	0.14	0.19	0.07	0.12	0.15	0.17	0.15	0.09	0.04	0.13	0.14	0.16	0.16	0.21	0.30	0.22	0.25	0.37	0.18	0.16	0.13

(Continued on following page)

10.3389/feart.2022.1000603

TABLE 1 (*Continued*) Major and trace element compositions of Laoshan granite.

Sample	LS-4001	LS-4002	LS-4003	LS-4004	LS-4005	LS-4006	LS-4007	LS-4008	LS-4009	LS-4101	LS-4102	LS-4103	LS-4104	LS-4105	LS-4106	LS-4107	LS-4108	LS-4109	LS-4110	LS-4111	LS-4112	LS-4113	LS-4114
Gd	4.23	4.99	4.93	4.49	5.57	4.69	4.34	4.94	5.31	3.00	3.86	2.13	2.00	2.69	2.57	2.37	3.67	5.12	3.08	4.53	2.30	2.81	1.66
Tb	0.65	0.79	0.76	0.68	0.83	0.80	0.70	0.62	0.88	0.44	0.54	0.34	0.25	0.33	0.33	0.34	0.46	0.80	1.41	0.70	0.50	0.53	0.24
Dy	4.58	5.41	5.34	4.88	5.48	5.13	4.37	4.42	5.30	3.44	3.55	2.70	2.17	2.48	2.64	2.77	3.35	5.24	3.18	5.13	3.05	3.29	2.14
Ho	0.91	1.14	1.01	0.88	1.00	1.04	0.97	0.92	1.08	0.77	0.78	0.58	0.55	0.58	0.49	0.67	0.82	1.16	0.72	1.14	0.70	0.74	0.45
Er	2.43	3.09	2.99	2.86	3.04	3.24	3.11	2.72	3.05	2.50	1.83	1.93	2.01	2.09	1.89	2.26	2.84	3.72	2.66	4.07	2.60	2.15	1.56
Tm	0.46	0.49	0.44	0.38	0.52	0.47	0.46	0.42	0.50	0.47	0.28	0.40	0.31	0.40	0.37	0.43	0.46	0.57	0.50	0.78	0.50	0.41	0.32
Yb	3.17	3.62	3.67	3.23	3.54	4.09	3.19	3.42	4.02	3.54	2.31	3.61	2.52	3.16	2.89	3.51	4.04	4.36	3.55	5.06	4.72	4.07	1.95
Lu	0.55	0.53	0.50	0.44	0.48	0.57	0.40	0.50	0.56	0.47	0.38	0.40	0.41	0.49	0.51	0.59	0.63	0.65	0.51	0.69	0.64	0.40	0.42
Hf	6.58	6.70	6.31	7.12	8.36	7.68	5.68	7.03	8.76	6.98	5.12	7.06	8.41	9.88	8.66	13.3	10.8	9.48	8.61	12.4	14.0	7.16	5.61
Ta	4.68	4.21	3.46	3.85	4.25	3.95	4.17	3.63	4.66	1.93	4.20	2.01	1.79	2.16	2.15	2.18	2.42	2.26	2.41	2.71	3.35	1.66	1.75
Pb	19.2	20.8	26.4	16.6	18.4	29.1	21.4	19.2	22.3	13.1	17.6	6.78	9.94	8.60	7.43	13.1	26.5	18.9	13.7	16.2	16.2	12.0	9.32
Th	16.3	17.9	17.1	16.9	18.6	18.2	16.7	17.3	19.4	16.1	13.1	15.6	16.0	24.6	22.6	28.1	21.3	15.4	21.9	20.1	37.0	15.4	15.1
U	1.90	2.13	1.62	2.24	1.90	2.29	1.93	1.87	2.17	4.89	1.79	3.44	3.43	3.59	2.85	2.99	5.28	4.06	3.26	4.93	4.60	5.90	2.72
$(La/Yb)_N$	9.94	7.83	9.59	9.67	9.68	7.55	7.85	9.35	8.23	6.82	12.03	5.26	7.32	8.19	8.39	6.87	5.07	7.47	7.01	6.60	6.09	4.62	7.93
Eu/Eu*	0.10	0.10	0.07	0.12	0.04	0.07	0.10	0.10	0.08	0.10	0.03	0.19	0.22	0.18	0.20	0.26	0.31	0.13	0.26	0.25	0.22	0.20	0.23
10000*Ga/Al	2.80	2.88	2.79	2.70	2.95	3.03	2.80	2.82	2.84	2.80	3.10	2.90	2.90	2.90	3.21	3.36	3.33	2.98	3.07	3.21	3.29	3.42	2.79
Zr+Nb+Ce+Y	303	316	316	293	353	345	266	305	354	319	236	279	312	343	321	440	343	432	353	426	443	272	215
Y/Nb	0.47	0.49	0.50	0.56	0.53	0.55	0.66	0.48	0.55	0.74	0.38	0.73	0.56	0.62	0.65	0.55	0.76	1.03	0.70	0.85	0.49	0.83	0.51
Ce/Nb	1.24	1.25	1.54	1.14	1.27	1.49	1.39	1.36	1.33	1.39	1.08	1.57	1.28	1.40	1.41	1.21	1.06	1.82	1.27	1.44	1.15	1.48	1.22
Yb/Ta	0.68	0.86	1.06	0.84	0.83	1.04	0.76	0.94	0.86	1.83	0.55	1.80	1.41	1.46	1.34	1.61	1.67	1.93	1.47	1.87	1.41	2.45	1.11
La/Nb	0.80	0.68	0.87	0.89	0.83	0.78	0.79	0.84	0.81	0.93	0.80	0.95	0.85	1.05	1.05	0.89	0.78	1.33	0.99	1.06	0.82	0.94	0.80

Wt% for major element and ppm for trace element.

10.3389/feart.2022.1000603

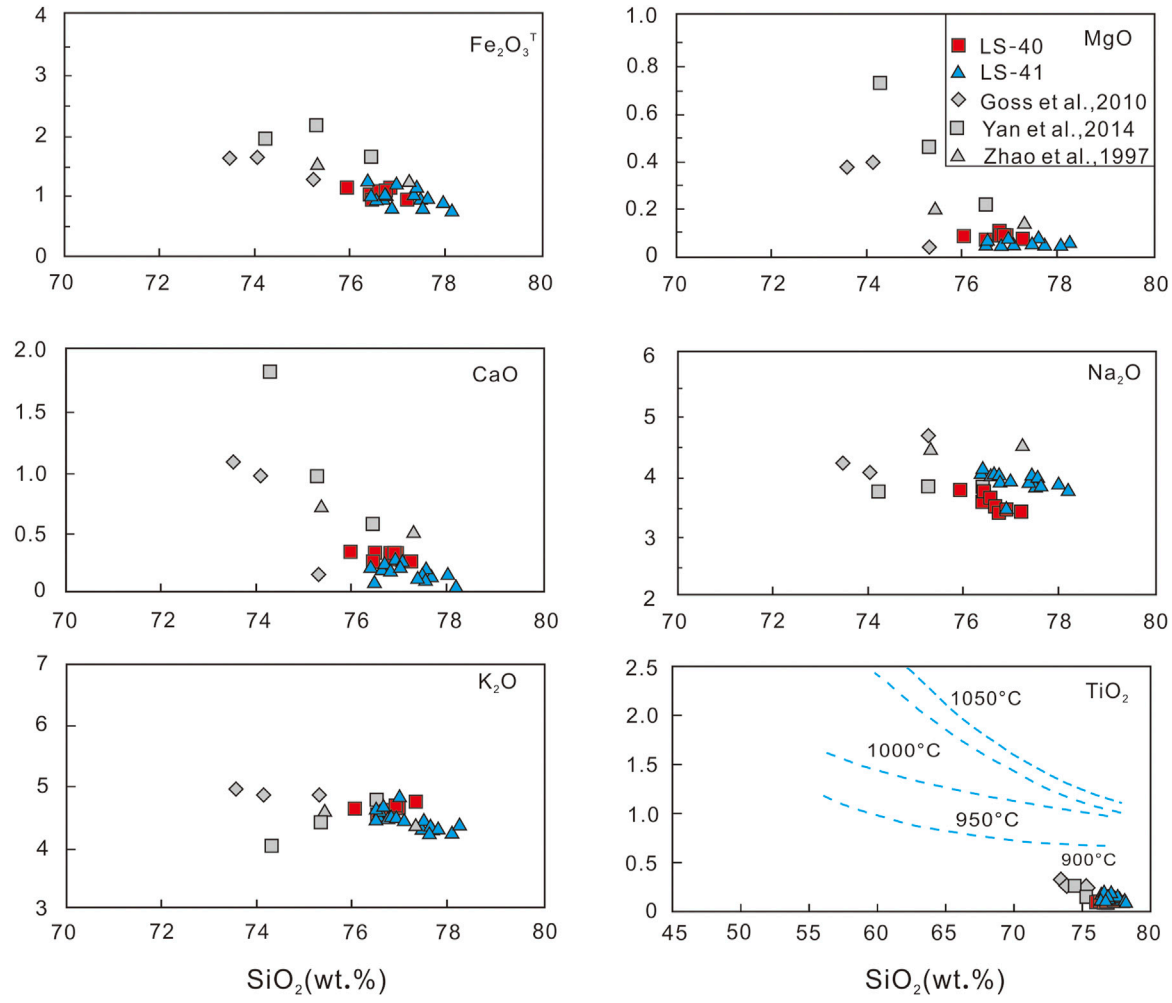

FIGURE 3
Harker diagrams for monzogranite, syenogranite, and alkali feldspar granite of the Laoshan granite complex. The monzogranite samples are from this article, and the data of Laoshan syenogranite and alkali feldspar granite are from references (Zhao et al., 1997; Goss et al., 2010; Yan and Shi, 2014).

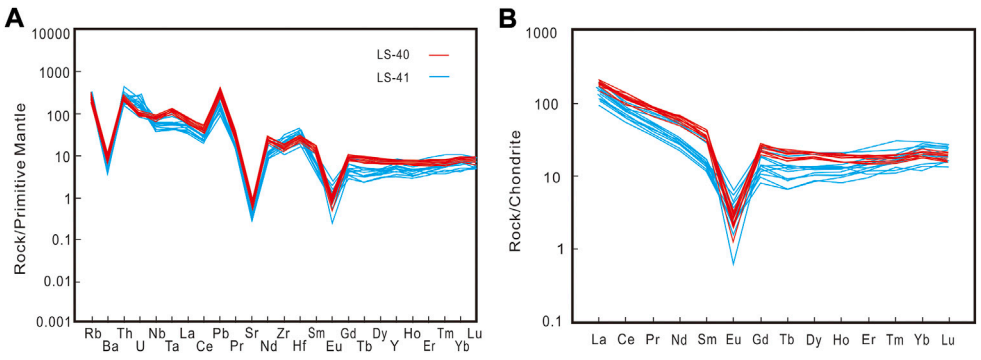

FIGURE 4
(A) Chondrite-normalized REE diagram. Chondritic values were from Sun and McDonough (1989). **(B)** Primitive mantle-normalized trace element diagram. Primitive mantle values are from Sun and McDonough (1989).

TABLE 2 LA-ICPMS zircon U–Pb data for Laoshan A-type granite (LS4002&LS4109).

Sample	$^{207}Pb/^{235}U$	$^{207}Pb/^{235}U$	$^{206}Pb/^{238}U$	$^{206}Pb/^{238}U$	$^{206}Pb/^{238}U$	$^{206}Pb/^{238}U$	Pb	Th	U	Ti	Th/U	Ce^{4+}/Ce^{3+}	T
	Ratio	2sigma	Ratio	2sigma	Age(Ma)	2sigma	ppm	ppm	ppm	ppm			°C
LS-4002-01	0.1163	0.0060	0.0178	0.0003	113.6	1.9	26.21	2042	973	4.69	2.10	76	740
LS-4002-02	0.1276	0.0078	0.0187	0.0004	119.3	2.7	10.40	757	339	8.73	2.23	54	801
LS-4002-03	0.1218	0.0059	0.0182	0.0003	116.5	1.9	20.42	1,199	814	6.52	1.47	40	771
LS-4002-04	0.1306	0.0075	0.0180	0.0004	115.2	2.5	7.68	329	344	4.24	0.96	46	730
LS-4002-05	0.1196	0.0083	0.0184	0.0005	117.7	2.9	7.67	381	315	5.10	1.21	67	748
LS-4002-06	0.1253	0.0054	0.0186	0.0003	118.8	2.0	14.90	448	684	1.90	0.66	33	662
LS-4002-07	0.1240	0.0074	0.0189	0.0004	120.5	2.3	12.14	406	562	3.68	0.72	43	718
LS-4002-08	0.1316	0.0078	0.0188	0.0004	120.0	2.5	13.08	684	491	3.97	1.39	102	725
LS-4002-09	0.1275	0.0102	0.0184	0.0006	117.3	3.7	6.60	300	267	5.38	1.13	98	753
LS-4002-10	0.1188	0.0098	0.0181	0.0004	115.9	2.8	9.88	762	325	11.44	2.34	32	830
LS-4002-11	0.1253	0.0062	0.0186	0.0003	119.0	1.8	22.47	644	1,037	2.22	0.62	79	675
LS-4002-12	0.1372	0.0075	0.0190	0.0004	121.1	2.8	23.22	1,059	943	6.04	1.12	14	764
LS-4002-13	0.1229	0.0092	0.0187	0.0005	119.3	3.0	15.17	821	596	7.55	1.38	49	786
LS-4002-14	0.1260	0.0106	0.0177	0.0005	113.3	3.0	4.04	161	182	6.75	0.89	181	775
LS-4002-15	0.1298	0.0099	0.0180	0.0004	114.9	2.6	9.27	607	344	6.62	1.76	113	773
LS-4002-16	0.1334	0.0070	0.0190	0.0004	121.2	2.4	37.87	2,845	1,146	9.06	2.48	45	805
LS-4002-17	0.1244	0.0119	0.0183	0.0006	116.6	3.6	3.88	104	186	2.43	0.56	75	682
LS-4002-18	0.1222	0.0066	0.0186	0.0004	118.5	2.4	12.10	365	565	3.27	0.65	112	707
LS-4002-19	0.1201	0.0059	0.0186	0.0003	118.6	2.2	16.21	595	725	5.44	0.82	123	754
LS-4002-20	0.1294	0.0075	0.0188	0.0004	120.4	2.6	11.60	289	536	3.48	0.54	8	713
LS-4002-21	0.1183	0.0056	0.0178	0.0004	113.5	2.2	18.71	403	931	2.72	0.43	130	691
LS-4002-22	0.1229	0.0075	0.0186	0.0004	118.6	2.4	27.94	1839	1,020	5.47	1.80	23	754
LS-4109-01	0.1211	0.0066	0.0186	0.0004	118.8	2.4	23.03	1,631	793	4.60	2.06	505	738
LS-4109-02	0.1208	0.0096	0.0184	0.0004	117.7	2.8	8.92	475	348	2.19	1.37	136	674
LS-4109-03	0.1252	0.0083	0.0189	0.0004	120.6	2.7	18.25	1,242	610	1.87	2.03	109	661
LS-4109-04	0.1264	0.0071	0.0191	0.0004	122.3	2.3	28.91	2,718	825	6.39	3.30	176	769
LS-4109-05	0.1201	0.0086	0.0183	0.0004	117.0	2.5	15.67	962	591	1.98	1.63	135	665
LS-4109-06	0.1207	0.0087	0.0180	0.0004	115.3	2.8	10.02	678	380	3.73	1.78	263	719
LS-4109-07	0.1219	0.0093	0.0187	0.0005	119.3	3.2	13.38	788	496	1.66	1.59	108	652
LS-4109-08	0.1302	0.0134	0.0187	0.0006	119.7	3.9	5.03	295	182	4.59	1.62	29	738
LS-4109-09	0.1336	0.0112	0.0189	0.0005	120.7	3.2	15.31	1,051	545	3.33	1.93	376	709
LS-4109-10	0.1273	0.0103	0.0187	0.0005	119.2	2.9	11.82	779	439	3.57	1.78	154	715

(Continued on following page)

10.3389/feart.2022.1000603

TABLE 2 (*Continued*) LA-ICPMS zircon U–Pb data for Laoshan A-type granite (LS4002&LS4109).

Sample	$^{207}Pb/^{235}U$		$^{207}Pb/^{235}U$	$^{206}Pb/^{238}U$		$^{206}Pb/^{238}U$		$^{206}Pb/^{238}U$	Pb	Th	U	Ti	Th/U	Ce^{4+}/Ce^{3+}	T
	Ratio		2sigma	Ratio		2sigma		Age(Ma)	2sigma	ppm	ppm	ppm			°C
LS-4109-11	0.1233		0.0082	0.0187		0.0004		119.7	2.7	19.64	1,158	700	5.00	1.66	76	746
LS-4109-12	0.1367		0.0086	0.0193		0.0004		122.9	2.7	43.09	3,678	1,298	6.58	2.83	359	772
LS-4109-13	0.1220		0.0108	0.0185		0.0005		118.0	3.3	10.67	707	382	2.54	1.85	48	686
LS-4109-14	0.1258		0.0107	0.0189		0.0005		120.8	3.2	21.62	1,474	717	2.54	2.05	379	686
LS-4109-15	0.1365		0.0145	0.0191		0.0006		121.7	3.8	10.58	1,013	279	7.21	3.63	41	781
LS-4109-16	0.1351		0.0094	0.0192		0.0004		122.9	2.7	22.74	1,578	785	2.25	2.01	1	676
LS-4109-17	0.1292		0.0098	0.0194		0.0005		123.8	3.1	11.61	633	414	4.28	1.53	258	731
LS-4109-18	0.1295		0.0108	0.0193		0.0005		123.4	3.1	12.40	716	449	3.11	1.60	128	703

log (Ti) = 5.711 ± 0.072 - 4,800(±86)/T(K) - log (aSiO2) + log (aTiO2) (Schiller and Finger, 2019; Yu et al., 2022).

Apatite major and trace elements

The apatites of the LS-40 sample have prismatic grains with smooth surface planes, indicating that they are magmatic apatite. The SiO_2 concentrations range from 0.21 wt% to 0.53 wt%, and the MnO concentrations range from 0.08 wt% to 0.30 wt%, which reflect the characteristics of the parent magma (Chen et al., 2017; Chen and Zhang, 2018; Sun et al., 2019; Yang et al., 2020c). The apatite major and trace elements show enriched fluorine (2.09–2.71 wt%) and low chlorine contents (0.01–0.09 wt%), with F/Cl ratios of 23.2–577 (Table 4). The apatites in these samples are enriched in LREEs ($(La/Yb)_N$ = 11.3 to 37.8; $(La/Gd)_N$ =3.07 to 8.31; $(Gd/Yb)_N$ =2.80–4.74) with a downwards sloping pattern toward HREEs (Figure 6). The apatite Ce/Pb ratios are 577–1,197, and Th/U ratios are 3.12–9.94.

Discussion

A-type granite affinity of the laoshan granite

A-type granite was originally used to describe the granite generated along rift zones and anorogenic environments (Loiselle and Wones, 1979). There is still debate about its petrogenesis and classification (Loiselle and Wones, 1979; Collins et al., 1982; Clemens et al., 1986; Whalen et al., 1987; Eby, 1990; Martin et al., 1994; Douce, 1997; King et al., 1997; Frost et al., 2001; Yang et al., 2006; Bonin, 2007; Huang et al., 2011). It is generally believed that A-type granite is derived from anhydrous and alkaline magma.

The geochemical compositions of A-type granite are characterized by enrichments in Na_2O + K_2O, REEs (except Eu), Nb, Ta, Zr and Ga, low MgO, CaO, Cr, Co, Ni, Sc, Sr, Ba, and Eu contents, and usually high $FeO^T/(FeO^T$ + MgO) ratios. Aluminous granites with depleted high field-strength elements may also plot in the VAG and WPG areas in the Rb–(Nb + Y) diagrams of Pearce and are classified as A-type granites (Pearce et al., 1984; Whalen et al., 1987; Bonin, 2007).

The major elements of the Laoshan granite display typical A-type granite characteristics, with high FeO^T/MgO ratios (11.6–33.6), K_2O/Na_2O ratios (1.08–1.39), K_2O + Na_2O (7.95–8.70 wt%), K_2O (4.23–4.79 wt%) and low P_2O_5 (0–0.01 wt%), CaO (0.04–0.33 wt%) contents (Figures 7A,B; Table 1; Frost et al., 2001).

The trace element compositions of the Laoshan granite also present A-type granite affinities. They are enriched in high field-strength elements (Zr, Y, Nb, Ta), with obvious depletions in Ba, Eu, Sr, and P. Low La/Nb ratios (mostly <1, except three samples 1.05–1.06) and high 10000*Ga/Al ratios (>2.6) are also consistent with typical A-type granite (Whalen et al., 1987).

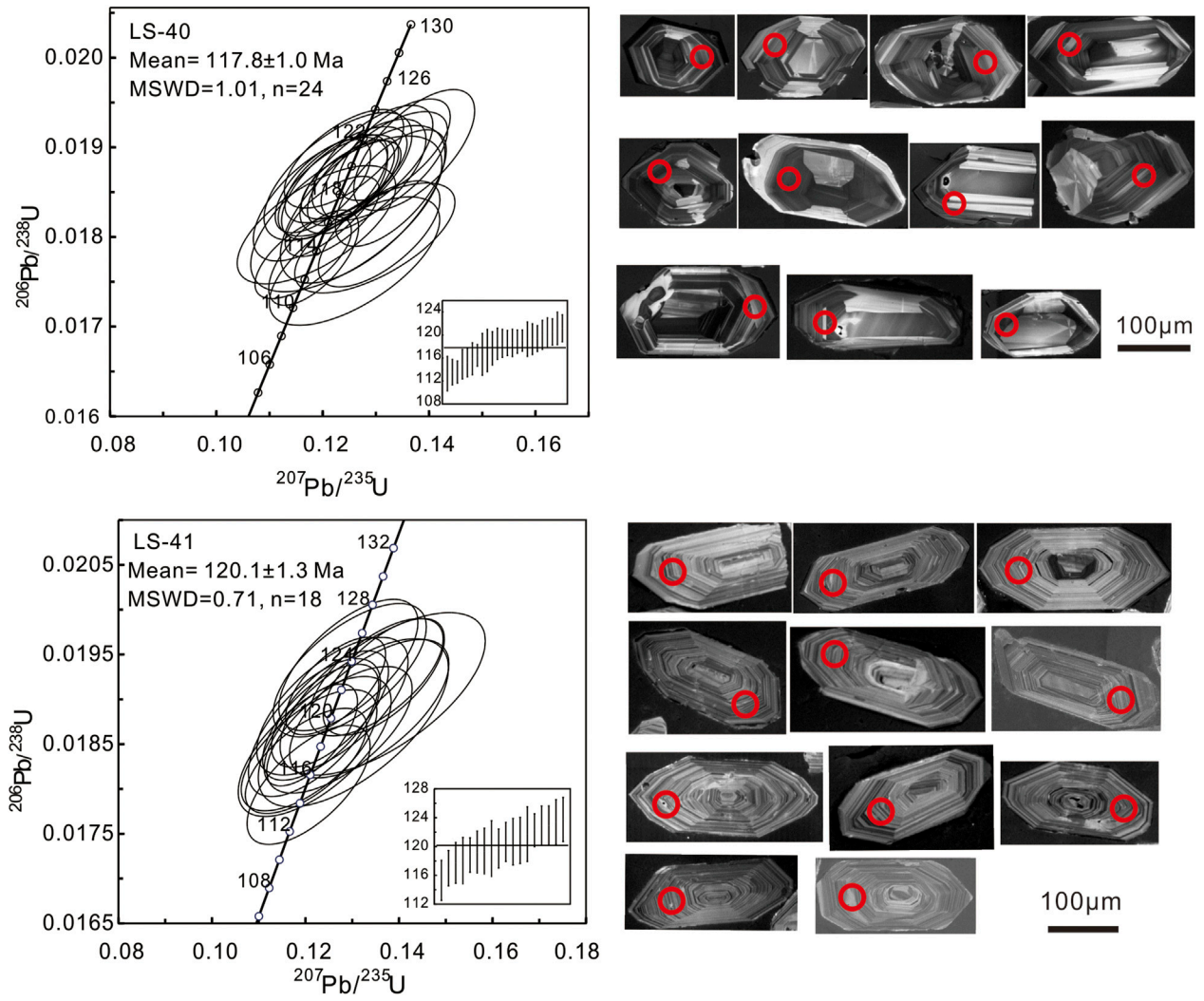

FIGURE 5
U–Pb concordia diagrams and cathodoluminescence (CL) image of zircons in monzogranites from the Laoshan granite. The average mean age of LS-41 is slightly older than that of LS-40.

A-type granite may contain low Zr, Nb, Ce, and Y because of extensive fractionation (Landenberger and Collins, 1996; Jiang et al., 2009), such that the effect of magmatic differentiation should be evaluated. Therefore, it is reliable to distinguish A-type granite by using these parameters. In addition, other discrimination diagrams based on key parameters also indicate that the Laoshan granite is an A-type granite (Figures 7C,D).

A-type granite has been further divided into A_1-type and A_2-type chemical subgroups (Eby, 1992). A_1-type granite has geochemical characteristics similar to those observed for oceanic island basalt (OIB) derived in an intraplate setting. In contrast, A_2-type granite has geochemical characteristics similar to those of rocks of island arc or continental crust origin located in a postcollisional setting (Eby, 1992). The arc signature of A_2-type granites has been considered to have been introduced through subduction-released fluids (Li et al., 2012a, 2014; Zhang et al., 2017b). The samples of Laoshan granite plot in the field of OIB (Figures 8A,B) and are classified as A_1-type granite based on high Nb and Ga relative to Ce and Y (Figures 8C,D). In addition, all the Y/Nb ratios of the Laoshan granite (0.38–1.03) are less than 1.2, supporting that it was derived from sources of oceanic island basalts (Eby, 1990). They plot in the field of within-plate type granite (WPG), and a few plot in the field of volcanic arc type granite (VAG) based on the diagram of Rb vs. (Y + Nb) (Figure 9).

Previous studies have shown that A_1-type and A_2-type granites form belts distributed parallel to each other in the LYR belt in eastern China (Figure 1C). This was explained by ridge subduction, which was also responsible for the genesis of

TABLE 3 Zircon trace element compositions for Laoshan A-type granite.

Sample	La (ppm)	Ce	Pr	Nd	Sm	Eu	Gd	Tb	Dy	Ho	Er	Tm	Yb	Lu	Hf	Ti
LS-4002-01	0.22	171	0.39	6.10	14.8	1.13	83.8	29.0	330	120	505	105	938	161	9,712	4.69
LS-4002-02	6.51	126	2.05	11.6	11.3	1.25	48.4	15.1	169	61.0	256	53.1	489	87.0	8,621	8.73
LS-4002-03	0.50	236	0.90	13.7	28.5	1.52	145	48.3	531	186	765	151	1,337	229	9,006	6.52
LS-4002-04	8.22	83.2	3.02	15.8	12.5	0.93	56.2	19.4	237	90.0	396	84.2	776	140	10,992	4.24
LS-4002-05	0.01	85.7	0.25	4.36	9.40	0.89	47.8	16.4	194	72.9	318	67.5	624	112	10,214	5.10
LS-4002-06	1.56	51.0	0.81	7.60	11.9	0.25	66.5	24.5	303	113	492	102	903	155	11,751	1.90
LS-4002-07	3.25	67.3	1.38	9.20	10.4	0.40	48.4	17.7	216	79.0	346	73.5	662	114	11,497	3.68
LS-4002-08	3.44	120	1.27	8.46	9.36	0.86	48.5	17.4	209	77.4	346	73.4	671	121	9,829	3.97
LS-4002-09	0.19	68.6	0.20	3.12	5.89	0.38	35.1	12.3	148	53.0	235	48.7	442	82.1	9,932	5.38
LS-4002-10	0.06	131	0.71	10.8	16.6	0.55	74.5	22.5	236	80.4	331	65.9	595	109	7,660	11.44
LS-4002-11	2.18	86.2	0.81	6.50	10.2	0.12	65.5	24.9	316	118	516	106	932	162	13,008	2.22
LS-4002-12	13.1	183	5.60	42.0	49.8	0.70	213	66.7	744	258	1,068	212	1859	330	9,494	6.04
LS-4002-13	0.60	138	0.49	7.09	15.9	0.73	81.1	27.3	311	111	471	93.6	826	149	10,563	7.55
LS-4002-14	0.01	73.2	0.14	2.56	5.43	0.66	29.6	11.3	144	59.3	279	62.3	603	117	9,584	6.75
LS-4002-15	0.04	102	0.21	3.54	7.38	0.94	42.7	14.7	172	62.9	276	57.7	530	99.3	9,280	6.62
LS-4002-16	0.25	421	1.18	20.4	41.4	3.07	192	61.8	687	240	1,003	199	1721	300	7,413	4.69
LS-4002-17	0.06	26.3	0.09	1.80	3.88	0.36	23.9	8.7	109	41.8	191	40.6	382	70.8	12,925	8.73
LS-4002-18	4.52	62.0	1.53	8.42	5.80	0.22	32.8	12.5	163	62.9	287	61.1	557	101	12,496	6.52
LS-4002-19	0.04	87.2	0.24	3.55	7.39	0.76	47.3	18.4	227	85.9	380	80.2	724	129	11,069	4.24
LS-4002-20	190	517	60.3	268	65.9	0.73	87.4	20.9	213	74.1	319	66.2	599	108	12,707	5.10
LS-4002-21	0.00	57.7	0.13	1.75	5.88	0.06	42.8	18.0	241	92.1	414	86.3	774	134	12,618	1.90
LS-4002-22	4.63	160	2.75	20.1	25.5	0.85	111	35.8	387	130	532	105	901	155	11,268	3.68
LS-4109-01	0.04	302	0.12	1.72	5.31	0.50	35.9	15.1	222	101	537	127	1,268	250	10,789	4.60
LS-4109-02	0.09	128	0.11	1.34	4.24	0.36	28.3	12.1	173	79.9	420	97.9	976	193	9,856	2.19
LS-4109-03	0.08	320	0.48	6.08	9.82	0.86	57.9	24.5	361	166	896	212	2090	413	10,831	1.87
LS-4109-04	0.00	335	0.19	3.81	11.6	1.69	79.6	29.3	360	141	629	128	1,119	201	9,315	6.39
LS-4109-05	0.00	219	0.11	1.42	3.33	0.40	25.0	12.5	193	96.1	531	131	1,319	264	9,606	1.98
LS-4109-06	0.00	183	0.24	3.30	5.80	0.45	34.6	15.2	225	108	595	144	1,427	284	11,593	3.73
LS-4109-07	0.08	203	0.16	3.01	6.81	0.60	40.0	17.4	249	114	585	133	1,293	251	9,762	1.66
LS-4109-08	0.04	117	0.18	3.73	7.40	1.01	46.2	17.5	218	88.3	410	87.0	793	146	10,032	4.59
LS-4109-09	2.46	225	0.71	4.51	7.52	0.72	47.3	18.9	252	105	503	111	1,041	197	10,175	3.33
LS-4109-10	0.00	239	0.28	4.34	8.31	0.90	53.8	23.2	320	143	739	169	1,660	323	10,691	3.57
LS-4109-11	0.01	298	0.10	1.89	4.59	0.65	37.8	17.1	247	115	609	142	1,397	276	9,482	5.00
LS-4109-12	0.03	613	0.20	3.01	7.91	0.77	52.3	22.8	344	161	873	206	2039	394	10,122	6.58
LS-4109-13	0.06	179	0.32	5.25	10.4	1.13	62.7	24.4	327	139	673	148	1,390	261	10,574	2.54
LS-4109-14	0.40	348	0.56	5.22	8.75	0.82	51.3	23.0	332	156	840	199	1972	389	9,584	2.54
LS-4109-15	0.37	624	3.20	54.3	108	11.34	457	136	1,377	432	1,588	276	2,142	352	6,778	7.21
LS-4109-16	0.43	348	0.29	2.29	5.36	0.57	38.4	17.0	257	122	659	157	1,563	303	9,037	2.25
LS-4109-17	0.00	159	0.13	1.69	4.79	0.64	33.0	13.7	195	85.4	438	100	966	190	9,812	4.28
LS-4109-18	0.03	166	0.10	1.46	3.70	0.43	27.2	12.3	185	87.5	466	112	1,104	219	9,341	3.11

adakites and copper-gold deposits there in the Early Cretaceous (Ling et al., 2009; Sun et al., 2010; Li et al., 2012a; Jiang et al., 2018). Geochemical studies on apatite from A_1-type and A_2-type granites in the LYR belt also showed systematic variations (Jiang et al., 2018). This ridge was moving northwards (Sun et al., 2007; Ling et al., 2013). The Early Cretaceous adakites and basalts in the Xuhuai and Shandong regions were explained as a result of ridge subduction in the Shandong Peninsula, which triggered the decratonization of the NCC (Ling et al., 2013; Wu et al., 2017). Many Early Cretaceous A-type granites crop out in this

TABLE 4 Major and trace element compositions of apatite from Laoshan granite samples.

Element	LS-4002-01	LS-4002-02	LS-4002-03	LS-4002-04	LS-4002-05	LS-4002-06	LS-4002-07	LS-4002-08	LS-4002-09	LS-4002-10	LS-4002-11	LS-4002-12	LS-4002-13
CaO	54.5	54.1	53.8	54.9	54.4	54.5	55.4	53.3	53.5	54.0	54.0	54.8	54.6
P_2O_5	42.5	42.4	41.3	42.3	42.6	42.6	41.9	42.3	41.2	43.0	43.0	43.1	41.8
SiO_2	0.38	0.26	0.56	0.22	0.27	0.37	0.44	0.28	0.53	0.21	0.21	0.26	0.38
FeO	0.05	0.04	0.05	0.15	0.07	0.09	0.12	0.47	0.11	0.16	0.06	0.05	0.06
MnO	0.23	0.25	0.20	0.20	0.14	0.30	0.10	0.23	0.27	0.25	0.20	0.08	0.23
MgO	0.01	0.00	0.01	0.02	0.00	0.01	0.02	0.01	0.02	0.00	0.01	0.01	0.01
SrO	0.00	0.00	0.02	0.00	0.02	0.00	0.03	0.01	0.01	0.00	0.02	0.03	0.00
F	2.72	2.58	2.71	2.52	2.59	2.68	2.09	2.35	2.61	2.31	2.66	2.27	2.42
Cl	0.01	0.04	0.02	0.03	0.04	0.03	0.09	0.04	0.03	0.00	0.01	0.04	0.02
Total	99.2	98.7	97.6	99.3	99.1	99.4	99.3	98.0	97.1	99.0	99.1	99.6	98.6
F/Cl	248	66.2	129	97.0	63.1	83.8	23.2	65.4	84.3	577	190	51.6	115
Rb	0.49	0.58	0.42	0.35	8.99	0.03	0.84	0.11	2.10	0.40	0.12	0.22	
Sr	36.7	168	39.7	41.3	60.6	43.5	1,572	337	174	42.3	34.3	1,341	
Y	3,568	1,383	2031	1994	1,453	2014	280	756	1,485	1,544	1930	476	
La	3,174	2,118	2,753	1779	2,404	2,191	499	2,386	1841	2,384	2,465	578	
Ce	8223	5,061	6,586	4,564	5,621	5,615	1,087	5,146	4,625	5,455	5,937	1,461	
Pr	1,079	617	811	591	668	715	134	588	590	653	730	174	
Nd	4,489	2,504	3,264	2,436	2,675	2,994	577	2,320	2,451	2,691	3,036	771	
Sm	1,047	493	660	568	519	621	107	359	511	515	607	150	
Eu	15.2	14.3	17.7	7.79	17.6	10.8	25.5	26.5	20.8	13.8	14.6	33.2	
Gd	896	389	530	477	379	480	83.1	249	388	394	482	124	
Tb	124	50.4	71.2	66.0	49.9	64.9	9.22	29.6	52.0	52.6	64.8	14.3	
Dy	716	280	409	385	285	381	47.7	163	288	287	367	80.1	
Ho	124	48.0	68.7	65.3	47.1	67.2	9.06	28.4	49.7	51.0	63.5	15.6	
Er	297	114	165	153	116	164	25.7	69.8	124	121	152	42.7	
Tm	35.0	13.5	19.8	18.4	13.2	19.5	3.38	8.49	15.4	14.2	18.2	5.74	
Yb	174	67.9	97.9	92.5	68.3	108	22.2	45.3	84.8	73.6	94.4	36.8	
Lu	19.9	8.31	11.5	11.7	7.94	13.6	3.31	5.81	10.8	8.47	11.05	5.39	

region. Similar to the A-type granites in the LYR belt, the A-type granites in the Shandong Peninsula have similar geochemical characteristics and distribution patterns.

Origin of the laoshan A-type granite

The Laoshan monzogranite is enriched in LILEs (such as Rb and Pb) and LREEs, pointing to LREE- and LILE-enriched sources. In the diagram of Ce/Pb vs. Nb/U, the LS-40 samples have systematically higher Nb/U ratios (21.8–34.7) than LS-41 (4.73–12.7, except for one sample of 27.0) with comparable Ce/Pb ratios (1.46–6.48) (Figure 10). The Nb/U and Ce/Pb ratios of LS-41 are lower than those of MORB and OIB (~25 and ~47, respectively) (Hofmann, 1997; Sun et al., 2008, 2013), but the Nb/U ratios of LS-41 are similar to those of the upper continental crust (~4.44), and the Ce/Pb ratios are equivalent to the average of the bulk continental crust (~3.91) (Rudnick and Gao, 2003). Nevertheless, the high temperatures of Laoshan A-type granites do not support direct continental crust origins. Given that Pb is more mobile than Ce, the lower Ce/Pb ratios indicate the influence of subduction-released fluids during plate subduction (McCulloch and Gamble, 1991; Pearce and Peate, 1995; Sun et al., 2008).

Apatite, containing volatiles and REEs, can provide information on metasomatic processes (Boyce and Hervig, 2008; Harlov, 2015) and petrogenetic processes that are usually obscure according to whole-rock geochemistry (Li et al., 2014; Miles et al., 2014; Bruand et al., 2017; Jiang et al., 2018). Apatite from the Laoshan granite contains low Cl and high F contents, indicating that the magmatic source of the Laoshan granite is characterized by low Cl and high F contents (Sun et al., 2019). During the evolution of granitic magma, most fluorine tends to enter crystallizing apatite, whereas there is a linear correlation between the Cl concentration of apatite and the concentration of Cl in the fluid (Webster et al., 2009).

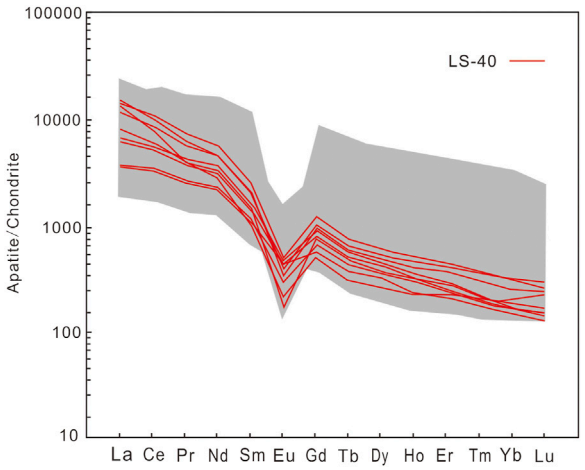

FIGURE 6
Apatite chondrite-normalized REE diagram for the Laoshan granite. Chondritic values were from Sun and McDonough (1989). All REEs have a decline to the right. Apatites of Laoshan granite have lower HREEs than Haiyang syenite and A-type granite in the LYR belt (gray area) (Li et al., 2014; Jiang et al., 2018).

During plate subduction, the majority of fluorine is retained in apatite and phengite (Sorensen et al., 1997), and it may be released during the rollback of a flatly subducting slab (Schmidt et al., 2004; Li et al., 2012a, 2014; Schmidt and Poli, 2014; Jiang et al., 2018). Cl is mainly hosted in amphibole, which tends to decompose at low pressure and release Cl into fluids at shallow depths (Volfinger et al., 1985; Zhang, 2012). The low Cl and high F contents may reflect that the source of the Laoshan granite involved fewer contributions from amphibole at shallow depths and more contributions from phengite (Figure 11).

Apatites from the Laoshan granite show mantle components in the source, as illustrated by the REE discrimination diagram (Figure 12) (Zhu et al., 2004), similar to those of the Haiyang syenite in the Shandong Peninsula and the A-type granite in the LYR belt (Li et al., 2014; Jiang et al., 2018).

Apatites in LS-40 samples are enriched in LREEs and depleted in HREEs with a right sloping pattern (Figure 6) with $(La/Yb)_N$ of 11.3–37.8, which is systematically lower than those from syenite and K-feldspar granite of Haiyang rock ($(La/Yb)_N$ = 22.5–64.0). The Ce/Pb ratios of apatites from Laoshan granite are similar to those of Huangmeijian (HMJ) A_1-type

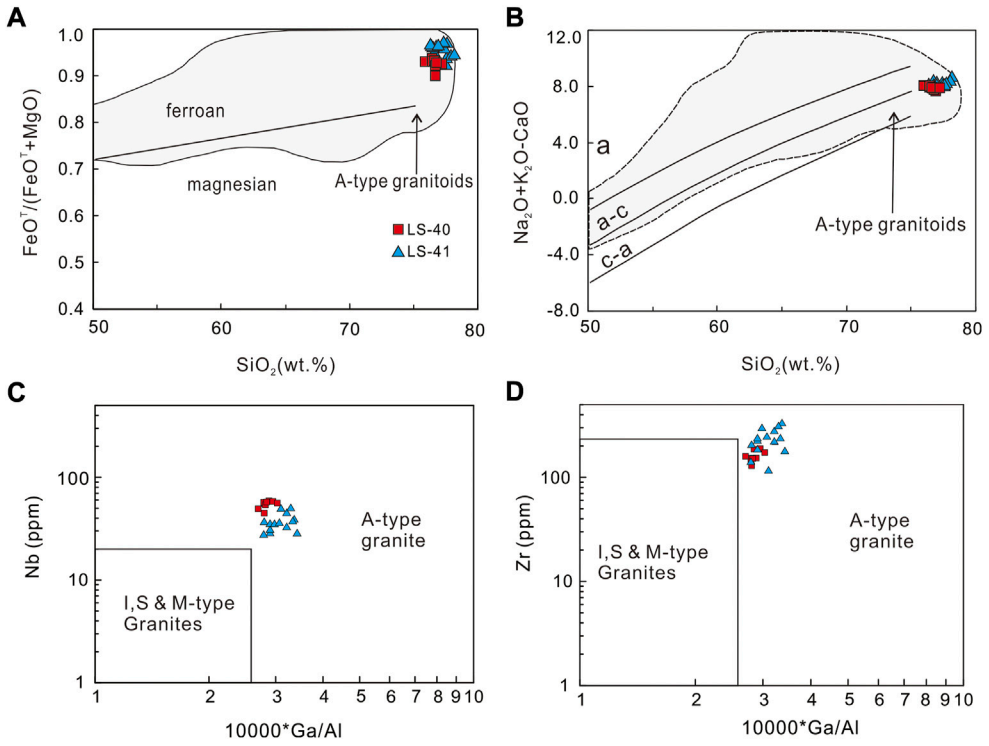

FIGURE 7
(A) FeOT/(FeOT + MgO) vs. SiO2 diagram, showing that all samples are ferroan granite A-type granites; **(B)**. K2O + Na2O−CaO vs. SiO2 discrimination diagram. Modified after Frost et al. (2001). **(C)** and **(D)** Various geochemical discrimination diagrams for A-type granite. Base maps are after Whalen et al. (1987) and Eby (1990).

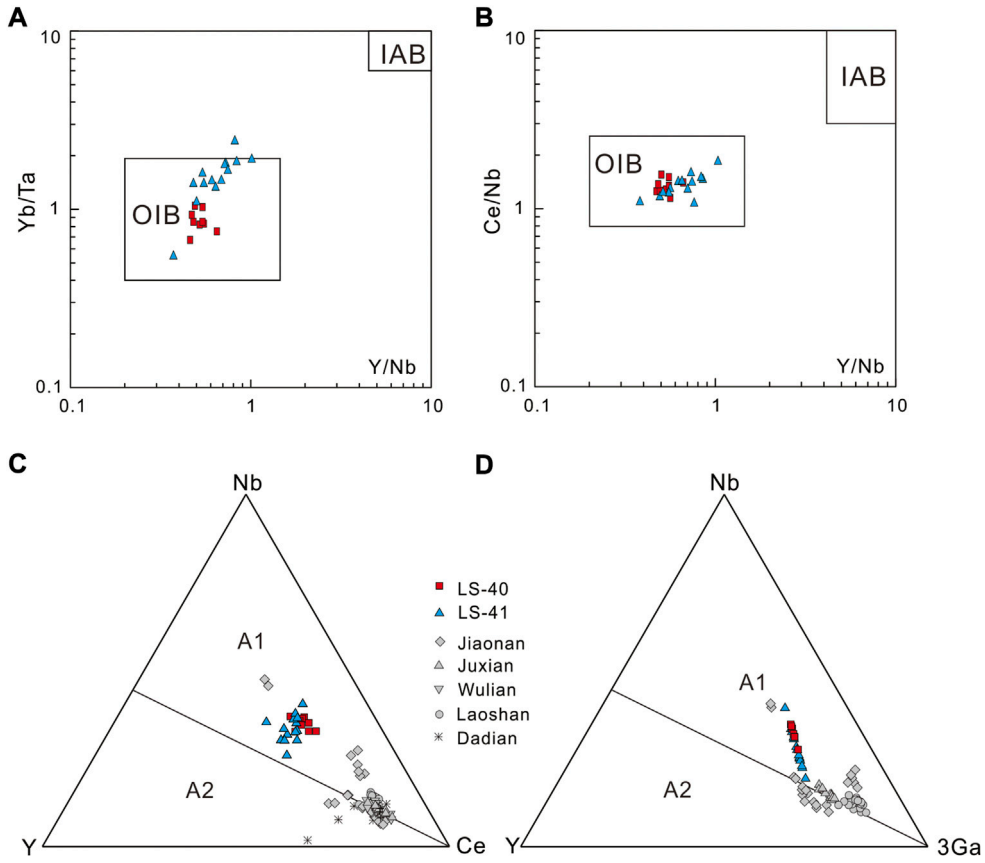

FIGURE 8
Representative geochemical diagrams for distinguishing between A1-type and A2-type granites. **(A)** Yb/Ta versus Y/Nb and **(B)** Ce/Nb versus Y/Nb diagrams for the Laoshan A-type granites. OIB = oceanic island basalt; IAB = island arc basalt. Base maps are after Eby (1992). In the **(C)** and **(D)** diagrams, the dashed line corresponds to Y/Nb ratios of 1.2 (Eby 1992). The data of the Laoshan pluton plot in the A1-type granite field; the data of the Haiyang, Juxian, Wulian and Jiaonan plutons plot near the line of demarcation of A1-type to A2-type granite (Zhao et al., 1997; Goss et al., 2010; Liu et al., 2013; Li et al., 2014; Yan and Shi 2014).

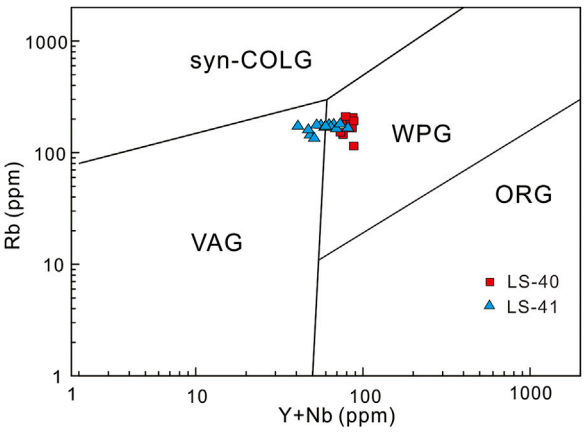

FIGURE 9
Tectonic setting discrimination diagram for granite (after Pearce et al., 1984). COLG = syncollisional granites; VAG = volcanic arc granites; ORG = ocean ridge granites; WPG =within-plate granites.

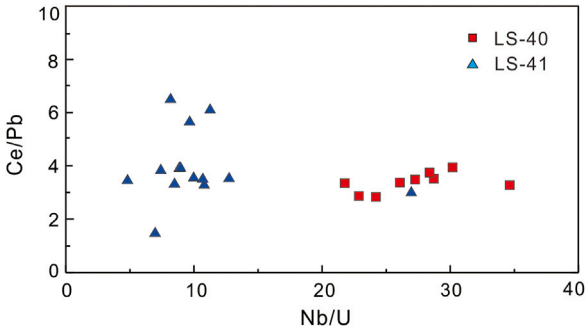

FIGURE 10
Ce/Pb vs. Nb/U ratio diagram, showing that LS-40 samples have higher Nb/U ratios than LS-41 but comparable Ce/Pb ratios.

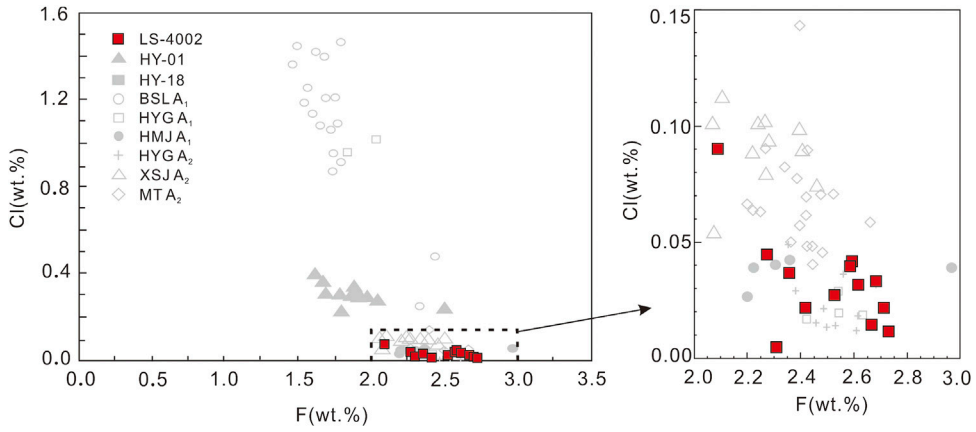

FIGURE 11
Cl vs. F diagram of the apatites, showing Laoshan granite with high F content and low Cl content. The apatite F-Cl composition of the Laoshan granite is similar to that of Huangmeijian (HMJ) A1-type granite in the LYR belt (Li et al., 2014; Jiang et al., 2018).

granite in the LYR belt. The Th/U ratios of samples from the Laoshan, Haiyang, and LYR belts are comparable. The Laoshan A_1-type granite is enriched in LREEs, similar to Huangmeijian (HMJ) A_1-type granite in the LYR belt (Debret et al., 2013; Jiang et al., 2018).

In the early stage of subduction, chrysotile transforms to antigorite and releases a large number of LREEs. As subduction continues, the antigorite transforms to secondary olivine, which contains much lower REEs. This results in higher LREE contents in the fluids released at the early stage (Debret et al., 2013) and may explain why apatites from the Laoshan A_1-type granite have higher $(Gd/Yb)_N$ and $(La/Yb)_N$ ratios but less variation in $(La/Gd)_N$ (Figure 13).

Cretaceous ridge subduction under the north China craton

The A-type granite belt in the Shandong Peninsula is NE-trending, including the Juxian, Wulian, Jiaonan, Laoshan, and Haiyang plutons, from southwest to northeast (Figure 1B). It can be further divided into A1-type and A1-A2 transitional-type granites (Figures 8C,D). The A1-type granite is mainly distributed in the Laoshan area, and the A1-A2 transitional type is distributed on both sides of the A1 granite, such as the Jiaonan, Juxian, Wulian and Haiyang areas (Figure 1B). All the A-type granites were formed at 110–123 Ma (Zhao et al., 1997; Goss et al., 2010; Liu et al., 2013; Li et al., 2014; Yan and Shi, 2014).

In the Early Cretaceous, the geodynamic setting in eastern China was mainly influenced by two subducting plates: the northwestward subducted Izanagi plate and the southwestward subducted Pacific plate (Maruyama et al., 2010). At ~125 Ma, the drifting direction of the Pacific plate changed to northwestward (Sun et al., 2007). Consequently, the ridge between these two plates moved northwards (Sun et al., 2007; Wu et al., 2017). This ridge moved westward and subducted to the Middle and Lower Yangtze River at approximately 140 Ma (Ling et al., 2009; Sun et al., 2010). Then, it moved to the Shandong Peninsula at ~120–130 Ma (Ling et al., 2009; Wu et al., 2017).

As subduction continued, the ridge gradually opened to form a slab window, and the asthenospheric material upwelled, forming A-type granite (Thorkelson and Breitsprecher, 2005; Li et al., 2011; Ling et al., 2011). Because the spreading oceanic ridge is hotter and drier than the normal oceanic crust, A1-type granite forms near the subducting ridge. The oceanic crust is increasingly wetter and colder with increasing distance from the oceanic ridge. Dehydration increases while partial melting decreases, forming A2-type granite during slab rollback (Ling et al., 2009, 2011; Li et al., 2011, 2014). Therefore, the distribution characteristics of A1-type and A2-type granites can be used to identify the locations of subduction ridges. This view has been well confirmed by the distribution of Mesozoic A-type granites in the LYR belt (Ling et al., 2009, 2013; Li et al., 2012a).

The mechanism of the destruction of the NCC has been debated for several decades. There are several competing models, including delamination (Wu et al., 2002; Gao et al., 2004), thermal erosion (Xu, 2007; Xu et al., 2014) and plate subduction (Niu, 2005; Sun et al., 2007; Zhu et al., 2011, 2012b, 2015). Previous studies have shown that ridge subduction at ~130 ± 5 Ma along the Xu-huai region and Shandong Peninsula was the key to the destruction of the NCC, and this subducting ridge migrated grandually northwards (Ling et al., 2013; Wu et al., 2017). Ridge subduction is usually flat with a strong power of physical erosion on the lithospheric mantle. Moreover, the duration of ridge subduction in Shandong Peninsula coincided with the peak of the destruction of the

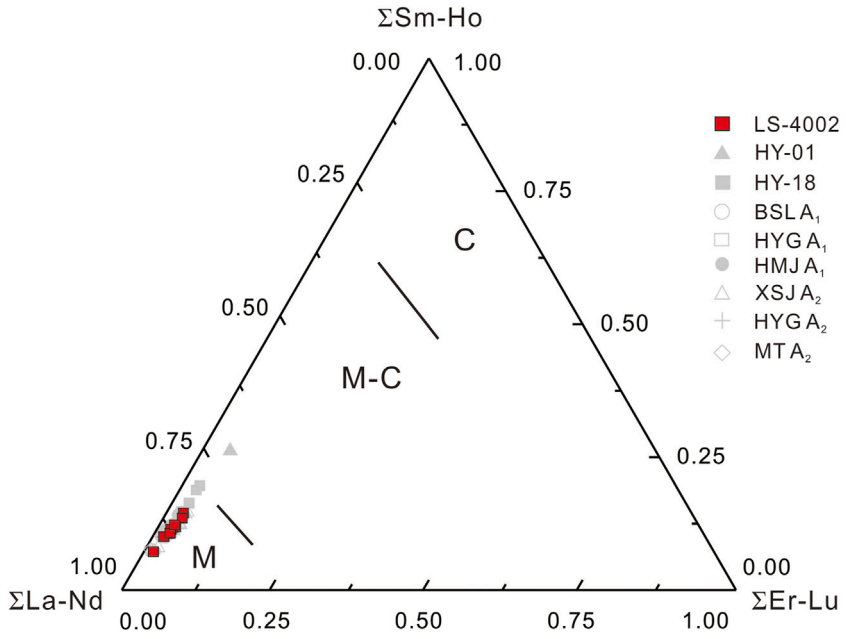

FIGURE 12
∑La~Nd−∑Sm~Ho−∑Er~Lu triangle diagram of the apatites, showing that the Laoshan granite has mantle components similar to those of the A-type granite in the LYR belt (Jiang et al., 2018). The Haiyang K-feldspar granite (HY-01) and syenite (HY-18) have major mantle contributions, with slight crustal addition (Li et al., 2014). M stands for mantle origin; M−C stands for mixing of mantle and crust origin; and C stands for crustal origin.

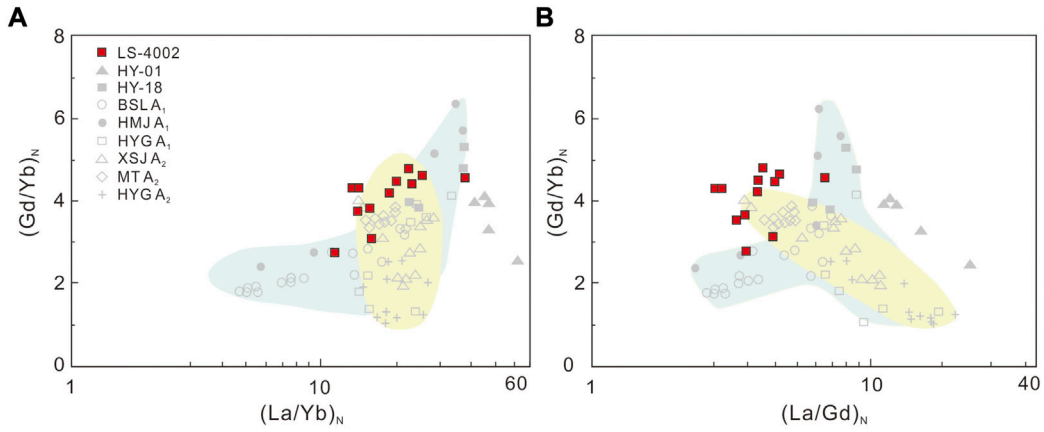

FIGURE 13
(A) (Gd/Yb)N versus (La/Yd)N, **(B)** (Gd/Yb)N versus (La/Gd)N diagrams of apatite from Laoshan A1-type granites. The gray figure represents A1- and A2-type granites in the LYR belt and the data after Jiang et al. (2018). The green field designates the A1-type granite, and yellow designates the A2-type granite.

NCC. This interpretation is supported by later studies that suggested that the advancing flat slab can scrape off the lowermost 20–50 km of continental mantle lithosphere (Axen et al., 2018). During the Early Cretaceous, the destruction of the NCC was followed by extensive granitic magmatic activity (Xu, 2001; Xu et al., 2004, 2012; Menzies et al., 2007; Yang et al., 2018b, 2020b). These intrusions, which record large-scale magmatic activity information, are important in revealing the geodynamic mechanism of eastern China. In particular, A-type granites, formed in extensional environments, can elucidate

regional tectonic settings (Loiselle and Wones, 1979; Whalen et al., 1987). Ridge subduction is usually flat, which is followed by slab rollback. Flat subduction and subsequent slab rollback can plausibly explain the destruction and subsequent large-scale magmatism in eastern China (Ling et al., 2013; Wu et al., 2017). Combined with the spatial distribution of the A-type granites in Shandong Peninsula and the drift history of the Izanagi plate in the Early Cretaceous, we propose that the Laoshan A-type granite and other A-type intrusions, i.e., the Haiyang A1-A2-type complex in Shandong Peninsula, were the result of ridge subduction.

Conclusion

The Laoshan granites formed at 117.8 ± 1.0 Ma to 120.1 ± 1.3 Ma. The geochemical characteristics indicate that the Laoshan plutons belong to A-type granites with high total alkali contents, high Ga/Al and FeO^T/MgO ratios, and LILE enrichments. It is further classified into the A_1 subgroup. It crystallized under moderate and low oxygen fugacity conditions, as indicated by zircon Ce^{IV}/Ce^{III} ratios. Apatites from Laoshan granites show high F and low Cl contents, with high $(Gd/Yb)_N$ and $(La/Yb)_N$ ratios, indicating influences from high F fluid in the source as the result of decomposition of the phengite in the subducted slab. The genesis of the A-type granite in the Shandong Peninsula can plausibly be interpreted with a ridge subduction model, which may have triggered the decratonization of the NCC.

Data availability statement

The raw data supporting the conclusions of this article will be made available by the authors, without undue reservation.

Author contributions

JL and HL conceived and designed the ideas. CL participated in field investigation. MS and LZ performed the data processing. MJ and reviewed and edited the draft, SY revised illustrations.

Funding

This study was supported by the National Natural Science Foundation of China (91958110) and the Strategic Priority Research Program of the Chinese Academy of Sciences (No. XDB42020203), the Hebei Natural Science Foundation (D2020403061), the Key Projects of Science and Technology Research in Universities of Hebei Province (ZD2021018), and the National Natural Science Foundation of China Shandong Joint Fund Project (U2006201).

Conflict of interest

The authors declare that the research was conducted in the absence of any commercial or financial relationships that could be construed as a potential conflict of interest.

Publisher's note

All claims expressed in this article are solely those of the authors and do not necessarily represent those of their affiliated organizations, or those of the publisher, the editors and the reviewers. Any product that may be evaluated in this article, or claim that may be made by its manufacturer, is not guaranteed or endorsed by the publisher.

References

Axen, G. J., Van Wijk, J. W., and Currie, C. A. (2018). Basal continental mantle lithosphere displaced by flat-slab subduction. *Nat. Geosci.* 11 (12), 961–964. doi:10.1038/s41561-018-0263-9

Ballard, J. R., Palin, J. M., and Campbell, I. H. (2002). Relative oxidation states of magmas inferred from Ce(IV)/Ce(III) in zircon: Application to porphyry copper deposits of northern Chile. *Contrib. Mineral. Pet.* 144, 347–364. doi:10.1007/s00410-002-0402-5

Belousova, E. A., Griffin, W. L., Suzanne, Y. O. R., and Fisher, N. I. (2002). Igneous zircon: Trace element composition as an indicator of source rock type. *Contrib. Mineral. Pet.* 143, 602–622. doi:10.1007/s00410-002-0364-7

Bonin, B. (2007). A-type granites and related rocks: Evolution of a concept, problems and prospects. *Lithos* 97, 1–29. doi:10.1016/j.lithos.2006.12.007

Boyce, J. W., and Hervig, R. L. (2008). Apatite as a monitor of late-stage magmatic processes at Volcán Irazú, Costa Rica. *Contrib. Mineral. Pet.* 157 (2), 135–145. doi:10.1007/s00410-008-0325-x

Bruand, E., Fowler, M., Storey, C., and Darling, J. (2017). Apatite trace element and isotope applications to petrogenesis and provenance. *Am. Mineralogist* 102, 75–84. doi:10.2138/am-2017-5744

Chen, L., Yan, Z., Wang, Z. Q., and Wang, K. M. (2017). Characteristics of apatite from 160-140 Ma Cu(Mo) and Mo(W) deposits in east qinling. *Acta Geol. Sin.* 91. 1925–19402.

Chen, L., and Zhang, Y. (2018). *In situ* major-trace-elements and Sr-Nd isotopic compositions of apatite from the luming porphyry Mo deposit, NE China: Constraints on the petrogenetic-metallogenic features. *Ore Geol. Rev.* 94, 93–103. doi:10.1016/j.oregeorev.2018.01.026

Clemens, J. D., Holloway, J. R., and White, A. J. R. (1986). Origin of an A-type granite; experimental constraints. *Am. Mineralogist* 7, 317–324.

Collins, W. J., Beams, S. D., White, A. J. R., and Chappell, B. W. (1982). Nature and origin of A-type granites with particular reference to southeastern Australia. *Contr. Mineral. Pet.* 80, 189–200. doi:10.1007/bf00374895

Debret, B., Nicollet, C., Andreani, M., Schwartz, S., and Godard, M. (2013). Three steps of serpentinization in an eclogitized oceanic serpentinization front (Lanzo Massif – western Alps). *J. Metamorph. Geol.* 31, 165–186. doi:10.1111/jmg.12008

Deng, J., Wang, C. M., Bagas, L., Carranza, E. M., and Lu, Y. J. (2015). Cretaceous-cenozoic tectonic history of the jiaojia fault and gold mineralization in the Jiaodong peninsula, China: Constraints from zircon U-Pb, illite K-Ar, and apatite fission track thermochronometry. *Min. Depos.* 50, 987–1006. doi:10.1007/s00126-015-0584-1

Deng, J., Wang, Q. F., Santosh, M., Liu, X. F., Liang, Y. Y., Yang, L. Q., et al. (2020). Remobilization of metasomatized mantle lithosphere: A new model for the Jiaodong gold province, eastern China. *Min. Depos.* 55 (3), 257–274. doi:10.1007/s00126-019-00925-0

Douce, A. E. P. (1997). Generation of metaluminous A-type granites by low-pressure melting of calc-alkaline granitoids. *Geol.* 25, 743–746. doi:10.1130/0091-7613(1997)025<0743:gomatg>2.3.co;2

Eby, G. N. (1992). Chemical subdivision of the A-type granitoids:Petrogenetic and tectonic implications. *Geol.* 20, 641–644. doi:10.1130/0091-7613(1992)020<0641:csotat>2.3.co;2

Eby, G. N. (1990). The A-type granitoids: A review of their occurrence and chemical characteristics and speculations on their petrogenesis. *Lithos* 26, 115–134. doi:10.1016/0024-4937(90)90043-z

Fan, H. R., Feng, K., Li, X. H., Hu, F. F., and Yang, K. F. (2016). Mesozoic gold mineralization in the Jiaodong and Korean peninsulas. *Acta Petrol. Sin.* 32, 3225–3238. (in Chinese with English abstract).

Fan, W. M., and Menzies, M. A. (1992). Destruction of aged lower lithosphere and accretion of asthenosphere mantle beneath eastern China. *Geotect. Metallogenia* 16, 171–180.

Frost, B. R., Barnes, C. G., Collins, W. J., Arculus, R. J., Ellis, D. J., and Frost, C. D. (2001). A geochemical classification for granitic rocks. *J. Petrology* 42, 2033–2048. doi:10.1093/petrology/42.11.2033

Gao, S., Rudnick, R. L., Yuan, H. L., Liu, X. M., Liu, Y. S., Xu, W. L., et al. (2004). Recycling lower continental crust in the North China craton. *Nature* 432, 892–897. doi:10.1038/nature03162

Gao, Y. J., Niu, Y. L., Duan, M., Xue, Q. Q., Sun, P., Chen, S., et al. (2019). The petrogenesis and tectonic significance of the Early Cretaceous intraplate granites in eastern China: The Laoshan granite as an example. *Lithos* 328–329, 200–211. doi:10.1016/j.lithos.2019.01.031

Goss, S. C., Wilde, S. A., Wu, F. Y., and Yang, J. H. (2010). The age, isotopic signature and significance of the youngest mesozoic granitoids in the Jiaodong Terrane, Shandong province, North China craton. *Lithos* 120, 309–326. doi:10.1016/j.lithos.2010.08.019

Groves, D. I., Zhang, L., and Santosh, M. (2020). Subduction, mantle metasomatism, and gold: A dynamic and genetic conjunction. *GSA Bull.* 132 (7-8), 1419–1426. doi:10.1130/b35379.1

Harlov, D. E. (2015). Apatite: A fingerprint for metasomatic processes. *Elements* 11, 171–176. doi:10.2113/gselements.11.3.171

Hofmann, A. W. (1997). Mantle geochemistry: The message from oceanic volcanism. *Nature* 385, 219–229. doi:10.1038/385219a0

Hoskin, P. W. O., and Black, L. P. (2000). Metamorphic zircon formation by solid-state recrystallization of protolith igneous zircon. *J. Metamorph. Geol.* 18, 423–439. doi:10.1046/j.1525-1314.2000.00266.x

Huang, H. Q., Li, X. H., Li, W. X., and Li, Z. X. (2011). Formation of high $\delta^{18}O$ fayalite-bearing A-type granite by high temperature melting of granulitic metasedimentary rocks, southern China. *Geology* 39, 903–906. doi:10.1130/g32080.1

Jiang, N., Zhang, S. Q., Zhou, W. G., and Liu, Y. S. (2009). Origin of a mesozoic granite with A-type characteristics from the north China craton: Highly fractionated from I-type magmas? *Contrib. Mineral. Pet.* 158, 113–130. doi:10.1007/s00410-008-0373-2

Jiang, X. Y., Li, H., Ding, X., Wu, K., Guo, J., Liu, J. Q., et al. (2018). formation of A-type granites in the lower Yangtze River belt: A perspective from apatite geochemistry. *Lithos* 304–307, 125–134. doi:10.1016/j.lithos.2018.02.005

King, P. L., White, A. J. R., Chappell, B. W., and Allen, C. M. (1997). Characterization and origin of aluminous A-type granites from the lachlan fold belt, southeastern Australia. *J. Petrology* 38, 371–391. doi:10.1093/petroj/38.3.371

Landenberger, B., and Collins, W. J. (1996). Derivation of A-type granites from a dehydrated charnockitic lower crust: Evidence from the chaelundi complex, eastern Australia. *J. Petrol.* 37, 145–170. doi:10.1093/petrology/37.1.145

Li, C. Y., Zhang, H., Wang, F. Y., Liu, J. Q., Sun, Y. L., Hao, X. L., et al. (2012b). The formation of the Dabaoshan porphyry molybdenum deposit induced by slab rollback. *Lithos* 150, 101–110. doi:10.1016/j.lithos.2012.04.001

Li, H., Ling, M. X., Ding, X., Zhang, H., Li, C. Y., Liu, D. Y., et al. (2014). The geochemical characteristics of Haiyang A-type granite complex in Shandong, eastern China. *Lithos* 200, 142–156. doi:10.1016/j.lithos.2014.04.014

Li, H., Ling, M. X., Li, C. Y., Zhang, H., Ding, X., Yang, X. Y., et al. (2012a). A-type granite belts of two chemical subgroups in central eastern China: Indication of ridge subduction. *Lithos* 150, 26–36. doi:10.1016/j.lithos.2011.09.021

Li, H., Zhang, H., Ling, M. X., Wang, F. Y., Ding, X., Zhou, J. B., et al. (2011). Geochemical and zircon U-Pb study of the huangmeijian A-type granite: Implications for geological evolution of the lower Yangtze River belt. *Int. Geol. Rev.* 53, 499–525. doi:10.1080/00206814.2010.496202

Li, J., Li, C. Y., Song, M. C., Liang, J. L., Zhang, L. P., and Song, Y. X. (2021). Mineralization of the shangjiazhuang Mo deposit in the Jiaodong peninsula, China: Constraints from S-H-O isotopes and fluid inclusions. *Solid Earth Sci.* 6 (4), 370–384. doi:10.1016/j.sesci.2021.08.001

Li, J., Song, M. C., Liang, J. L., Jiang, M. Y., Li, S. Y., Ding, Z. J., et al. (2020). Source of ore-forming fluids of the Jiaojia deeply-seated gold deposit: Evidences from trace elements and sulfur-helium-argon isotopes of pyrite. *Acta Petrol. Sin.* 36 (1), 297–313. (in Chinese with English abstract). doi:10.18654/1000-0569/2020.01.23

Li, S. G., Xiao, Y. L., Liou, D. L., Chen, Y. Z., Ge, N. J., Zhang, Z. Q., et al. (1993). Collision of the North China and Yangtse blocks and formation of coesite-bearing eclogites; timing and processes. *Chem. Geol.* 109, 89–111. doi:10.1016/0009-2541(93)90063-o

Li, X. H., Qi, C. S., Liu, Y., Liang, X. R., Tu, X. L., Xie, L. W., et al. (2005). Petrogenesis of the Neoproterozoic bimodal volcanic rocks along the Western margin of the Yangtze Block: New constraints from Hf isotopes and Fe/Mn ratios. *Chin. Sci. Bull.* 50, 2481–2486. doi:10.1360/982005-287

Liang, H. Y., Campbell, I. H., Allen, C., Sun, W. D., Liu, C. Q., Yu, H. X., et al. (2006). Zircon Ce^{4+}/Ce^{3+} ratios and ages for Yulong ore-bearing porphyries in eastern Tibet. *Min. Depos.* 41, 152–159. doi:10.1007/s00126-005-0047-1

Liang, J. L., Ding, X., Sun, X. M., Zhang, Z. M., Zhang, H., and Sun, W. D. (2009). Nb/Ta fractionation observed in eclogites from the Chinese continental scientific drilling Project. *Chem. Geol.* 268, 27–40. doi:10.1016/j.chemgeo.2009.07.006

Lin, J., Liu, Y. S., Yang, Y. H., and Hu, Z. C. (2016). Calibration and correction of LA-ICP-MS and LA-MC-ICP-MS analyses for element contents and isotopic ratios. *Solid Earth Sci.* 1, 5–27. doi:10.1016/j.sesci.2016.04.002

Ling, M. X., Li, Y., Ding, X., Teng, F. Z., Yang, X. Y., Fan, W. M., et al. (2013). Destruction of the north China craton induced by ridge subductions. *J. Geol.* 121, 197–213. doi:10.1086/669248

Ling, M. X., Wang, F. Y., Ding, X., Hu, Y. H., Zhou, J. B., Zartman, R. E., et al. (2009). Cretaceous ridge subduction along the lower Yangtze River Belt, eastern China. *Econ. Geol.* 104, 303–321. doi:10.2113/gsecongeo.104.2.303

Ling, M. X., Wang, F. Y., Ding, X., Zhou, J. B., and Sun, W. D. (2011). Different origins of adakites from the dabie mountains and the lower Yangtze River belt, eastern China: Geochemical constraints. *Int. Geol. Rev.* 53, 727–740. doi:10.1080/00206814.2010.482349

Liu, S., Feng, G. Y., Qi, Y. Q., Gao, S., Wang, T., et al. (2013). Zircon U-Pb age, geochemical, and Sr-Nd-Pb isotopic constraints on the;origin of alkaline intrusions in eastern Shandong Province, China. *Mineral. Pet.* 107, 591–608. doi:10.1007/s00710-013-0285-3

Liu, Y. S., Gao, S., Hu, Z. C., Gao, C. G., Zong, K. Q., and Wang, D. B. (2010). Continental and oceanic crust recycling-induced melt-peridotite interactions in the trans-north China orogen: U-Pb dating, Hf isotopes and trace elements in zircons from mantle xenoliths. *J. Petrology* 51, 537–571. doi:10.1093/petrology/egp082

Liu, Y. S., Hu, Z. C., Gao, S., Gunther, D., Xu, J., Gao, C. G., et al. (2008). *In situ* analysis of major and trace elements of anhydrous minerals by LA-ICP-MS without applying an internal standard. *Chem. Geol.* 257, 34–43. doi:10.1016/j.chemgeo.2008.08.004

Loiselle, M. C., and Wones, D. R. (1979). *Characteristics and origin of anorogenic granites*. New York: Geological society of America abstracts with programs, 468.

Martin, H., Bonin, B., Capdevila, R., Jahn, B. M., Lameyre, J., and Wang, Y. (1994). The kuiqi peralkaline granitic complex (SE China): Petrology and geochemistry. *J. Petrology* 35, 983–1015. doi:10.1093/petrology/35.4.983

Maruyama, S., Isozaki, Y., Kimura, G., and Terabayashi, M. (2010). Paleogeographic maps of the Japanese Islands: Plate tectonic synthesis from 750 Ma to the presen. *Isl. Arc* 6, 121–142.

McCulloch, M. T., and Gamble, J. A. (1991). Geochemical and geodynamical constraints on subduction zone magmatism. *Earth Planet. Sci. Lett.* 102, 358–374. doi:10.1016/0012-821x(91)90029-h

Menzies, M., Xu, Y. G., Zhang, H. F., and Fan, W. M. (2007). Integration of geology, geophysics and geochemistry: A key to understanding the north China craton. *Lithos* 96, 1–21. doi:10.1016/j.lithos.2006.09.008

Miles, A. J., Graham, C. M., Hawkesworth, C. J., Gillespie, M. R., Hinton, R. W., and Bromiley, G. D. (2014). Apatite: A new redox proxy for silicic magmas? *Geochimica Cosmochimica Acta* 132, 101–119. doi:10.1016/j.gca.2014.01.040

Niu, Y. L. (2005). Generation and evolution of basaltic magmas: Some basic concepts and a new view on the origin of mesozoic-cenozoic basaltic volcanism in eastern China. *Geol. J. China Univ.* 11, 9–46.

Pearce, J. A., Harris, N. B. W., and Tindle, A. G. (1984). Trace element discrimination diagrams for the tectonic interpretation of granitic rocks. *J. Petrology* 25, 956–983. doi:10.1093/petrology/25.4.956

Pearce, J. A., and Peate, D. W. (1995). Tectonic implications of the composition of volcanic arc magmas. *Annu. Rev. Earth Planet. Sci.* 23, 251–285. doi:10.1146/annurev.ea.23.050195.001343

Rudnick, R. L., and Gao, S. (2003). "Composition of the continental crust," in *Treatise on geochemistry*. Editor R. L. Rudnick (Elsevier), 1–64.

Schiller, D., and Finger, F. (2019). Application of Ti-in-zircon thermometry to granite studies: Problems and possible solutions. *Contrib. Mineral. Pet.* 174, 51. doi:10.1007/s00410-019-1585-3

Schmidt, M. W., and Poli, S. (2014). "Devolatilization during subduction," in *The crust. Treatise on geochemistry*. Editors R. L. Rudnick, H. D. Holland, and K. K. Turekian. Second edition (Oxford: Elsevier-Pergamon), 669–701.

Schmidt, M. W., Vielzeuf, D., and Auzanneau, E. (2004). Melting and dissolution of subducting crust at high pressures: The key role of white mica. *Earth Planet. Sci. Lett.* 228, 65–84. doi:10.1016/j.epsl.2004.09.020

Song, M. C., Li, J., Yu, X. F., Song, Y. X., Ding, Z. J., and Li, S. Y. (2021). Metallogenic characteristics and tectonic setting of the Jiaodong gold deposit, China. *Solid Earth Sci.* 6 (4), 385–405. doi:10.1016/j.sesci.2021.07.002

Song, M. C., Li, S. Z., Santosh, M., Zhao, S. J., Yu, S., Yi, P. H., et al. (2015). Types, characteristics and metallogenesis of gold deposits in the Jiaodong peninsula, eastern North China craton. *Ore Geol. Rev.* 65, 612–625. doi:10.1016/j.oregeorev.2014.06.019

Song, M. C., Wang, S. S., Yang, L. X., Li, J., Li, S. Y., and Ding, Z. J. (2017). Metallogenic epoch of nonferrous metallic and silver deposits in the Jiaodong peninsula, China and its geological significance. *Acta Geol. Sin. - Engl. Ed.* 91 (4), 1305–1325. doi:10.1111/1755-6724.13363

Song, M. C., Zhou, J. B., Song, Y. X., Wang, B., Li, S. Y., Li, J., et al. (2019). Mesozoic Weideshan granitoid suite and its relationship to large-scale gold mineralization in the Jiaodong Peninsula, China. *Geol. J.* 55 (8), 5703–5724. doi:10.1002/gj.3607

Sorensen, S. S., Grossman, J. N., and Perfit, M. R. (1997). Phengite-hosted LILE enrichment in eclogite and related rocks: Implications for fluid-mediated mass transfer in subduction zones and arc magma Genesis. *J. Petrology* 38, 3–34. doi:10.1093/petroj/38.1.3

Sun, S. J., Yang, X. Y., Wang, G. J., Sun, W. D., Zhang, H., Li, C. Y., et al. (2019). *In situ* elemental and Sr-O isotopic studies on apatite from the Xu-Huai intrusion at the southern margin of the North China Craton: Implications for petrogenesis and metallogeny. *Chem. Geol.* 510, 200–214. doi:10.1016/j.chemgeo.2019.02.010

Sun, S. S., and McDonough, W. F. (1989). "Chemical and isotopic systematics of oceanic basalts: Implications formantle composition andprocesses," in *Magmatism in the ocean basalts*. Editors A. D. Saunders and M. J. Norry (Geological Society, London: Special Publications), 313–345.

Sun, W. D., Ding, X., Hu, Y. H., and Li, X. H. (2007). The golden transformation of the Cretaceous plate subduction in the west Pacific. *Earth Planet. Sci. Lett.* 262, 533–542. doi:10.1016/j.epsl.2007.08.021

Sun, W. D., Hu, Y. H., Kamenetsky, V. S., Eggins, S. M., Chen, M., and Arculus, R. J. (2008). Constancy of Nb/U in the mantle revisited. *Geochimica Cosmochimica Acta* 72, 3542–3549. doi:10.1016/j.gca.2008.04.029

Sun, W. D., Li, S. G., Chen, Y. D., and Li, Y. J. (2002a). Timing of synorogenic granitoids in the south qinling, central China: Constraints on the evolution of the qinling-dabie orogenic belt. *J. Geol.* 110, 457–468. doi:10.1086/340632

Sun, W. D., Li, S., Yang, X. Y., Ling, M. X., Ding, X., Duan, L. A., et al. (2013). Large-scale gold mineralization in eastern China induced by an Early Cretaceous clockwise change in Pacific plate motions. *Int. Geol. Rev.* 55, 311–321. doi:10.1080/00206814.2012.698920

Sun, W. D., Ling, M. X., Yang, X. Y., Fan, W. M., Ding, X., and Liang, H. Y. (2010). Ridge subduction and porphyry copper-gold mineralization: An overview. *Sci. China Earth Sci.* 53, 475–484. doi:10.1007/s11430-010-0024-0

Sun, W. D., Williams, I. S., and Li, S. G. (2002b). Carboniferous and triassic eclogites in the Western dabie mountains, east-central China: Evidence for protracted convergence of the north and south China blocks. *J. Metamorph. Geol.* 20, 873–886. doi:10.1046/j.1525-1314.2002.00418.x

Tan, J., Wei, J. H., Audétat, A., and Pettke, T. (2012). Source of metals in the Guocheng gold deposit, Jiaodong Peninsula, North China Craton: Link to early Cretaceous mafic magmatism originating from Paleoproterozoic metasomatized lithospheric mantle. *Ore Geol. Rev.* 48, 70–87. doi:10.1016/j.oregeorev.2012.02.008

Thorkelson, D. J., and Breitsprecher, K. (2005). Partial melting of slab window margins: Genesis of adakitic and non-adakitic magmas. *Lithos* 79, 25–41. doi:10.1016/j.lithos.2004.04.049

Tu, X. L., Zhang, H. F., Deng, W. F., Liang, H. Y., and Sun, W. D. (2011). Application of RESOlution laser ablation ICPMS in trace element analyses. *Geochimica* 40, 83–98. (in Chinese with English abstract).

Volfinger, M., Robert, J. L., Vielzeuf, D., and Neiva, A. M. R. (1985). Structural control of the chlorine content of OH-bearing silicates (micas and amphiboles). *Geochimica Cosmochimica Acta* 49, 37–48. doi:10.1016/0016-7037(85)90189-9

Wang, D. Z., Zhao, G. T., and Qiu, J. S. (1995). The Tectonic constraint on the late mesozoic A-type granitoids in eastern China. *Geol. J. Univ.* 1, 13–21. (in Chinese with English abstract).

Wang, T., Liu, S., Hu, R. Z., Feng, C. X., Qi, Y. Q., Feng, G. Y., et al. (2009). Elemental geochemistry and petrogenesis of A-type granites in the sulu orogen. *J. Jilin Univ. Earth Sci. Ed.* 39, 676–688. (in Chinese with English abstract).

Webster, J. D., Tappen, C. M., and Mandeville, C. W. (2009). Partitioning behavior of chlorine and fluorine in the system apatite-melt-fluid. II: Felsic silicate systems at 200 MPa. *Geochimica Cosmochimica Acta* 73, 559–581. doi:10.1016/j.gca.2008.10.034

Whalen, J. B., Currie, K. L., and Chappell, B. W. (1987). A-type granites geochemical characteristics, discrimination and petrogenesis. *Contrib. Mineral. Pet.* 95, 407–419. doi:10.1007/bf00402202

Wu, F. Y., Lin, J. Q., Wilde, S. A., Zhang, X. O., and Yang, J. H. (2005). Nature and significance of the Early Cretaceous giant igneous event in eastern China. *Earth Planet. Sci. Lett.* 233, 103–119. doi:10.1016/j.epsl.2005.02.019

Wu, F. Y., Sun, D. Y., Li, H. M., Jahn, B. M., and Wilde, S. (2002). A-Type granites in northeastern China: Age and geochemical constraints on their petrogenesis. *Chem. Geol.* 187, 143–173. doi:10.1016/s0009-2541(02)00018-9

Wu, K., Ling, M. X., Sun, W. D., Guo, J., and Zhang, C. C. (2017). Major transition of continental basalts in the early cretaceous: Implications for the destruction of the north China craton. *Chem. Geol.* 470, 93–106. doi:10.1016/j.chemgeo.2017.08.025

Xie, J. C., Yang, X. Y., Sun, W. D., Du, J. G., Xu, W., Wu, L. B., et al. (2009). Geochronological and geochemical constraints on formation of the Tongling metal deposits, middle Yangtze metallogenic belt, east-central China. *Int. Geol. Rev.* 51, 388–421. doi:10.1080/00206810802712004

Xu, Y. G. (2007). Diachronous lithospheric thinning of the North China Craton and formation of the Daxin'anling–Taihangshan gravity lineament. *Lithos* 96, 281–298. doi:10.1016/j.lithos.2006.09.013

Xu, Y. G., Huang, X. L., Ma, J. L., Wang, Y. B., IizukaXu, Y. J. F., Wang, Q., et al. (2004). Crust-mantle interaction during the tectono-thermal reactivation of the north China craton: Constraints from SHRIMP zircon U-Pb chronology and geochemistry of mesozoic plutons from Western Shandong. *Contrib. Mineral. Pet.* 147, 750–767. doi:10.1007/s00410-004-0594-y

Xu, Y. G. (2001). Thermo-tectonic destruction of the archaean lithospheric keel beneath the Sino-Korean Craton in China: Evidence, timing and mechanism. *Phys. Chem. Earth Part A Solid Earth Geodesy* 26, 747–757. doi:10.1016/s1464-1895(01)00124-7

Xu, Y. G., Wei, X., Luo, Z. Y., Liu, H. Q., and Cao, J. (2014). The early permian tarim large igneous province: Main characteristics and a plume incubation model. *Lithos* 204, 20–35. doi:10.1016/j.lithos.2014.02.015

Xu, Y. G., Zhang, H. H., Qiu, H. N., Ge, W. C., and Wu, F. Y. (2012). Oceanic crust components in continental basalts from Shuangliao, Northeast China: Derived from the mantle transition zone. *Chem. Geol.* 328, 168–184. doi:10.1016/j.chemgeo.2012.01.027

Yan, Q. S., and Shi, X. F. (2014). Geochemistry and petrogenesis of the Cretaceous A-type granites in the Laoshan granitic complex, eastern China. *Isl. Arc* 23, 221–235. doi:10.1111/iar.12070

Yang, F., Santosh, M., Glorie, S., Jepson, G., Xue, F., and Kim, S. W. (2020a). Meso-cenozoic multiple exhumation in the Shandong peninsula, eastern North China craton: Implications for lithospheric destruction. *Lithos* 370-371, 105597. doi:10.1016/j.lithos.2020.105597

Yang, F., Santosh, M., Glorie, S., Xue, F., Zhang, S., and Zhang, X. (2020c). Apatite geochronology and chemistry of luanchuan granitoids in the east qinling orogen, China: Implications for petrogenesis, metallogenesis and exploration. *Lithos* 378, 105797. doi:10.1016/j.lithos.2020.105797

Yang, F., Santosh, M., and Kim, S. W. (2018a). Mesozoic magmatism in the eastern North China Craton: Insights on tectonic cycles associated with progressive craton destruction. *Gondwana Res.* 60, 153–178. doi:10.1016/j.gr.2018.04.003

Yang, F., Santosh, M., Kim, S. W., Zhou, H., and Jeong, Y. J. (2020b). Late mesozoic intraplate rhyolitic volcanism in the north China craton: Far-field effect of the westward subduction of the paleo-Pacific plate. *GSA Bull.* 132, 291–309. doi:10.1130/b35123.1

Yang, F., Santosh, M., and Tang, L. (2018b). Extensive crustal melting during craton destruction: Evidence from the Mesozoic magmatic suite of Junan, eastern North China Craton. *J. Asian Earth Sci.* 157, 119–140. doi:10.1016/j.jseaes.2017.07.010

Yang, J. H., Wu, F. Y., Chung, S. L., Wilde, S. A., and Chu, M. F. (2006). A hybrid origin for the qianshan A-type granite, northeast China: Geochemical and Sr–Nd–Hf isotopic evidence. *Lithos* 89, 89–106. doi:10.1016/j.lithos.2005.10.002

Yang, J. H., Wu, F. Y., Chung, S. L., Wilde, S. A., Chu, M. F., Lo, C. H., et al. (2005). Petrogenesis of Early Cretaceous intrusions in the Sulu ultrahigh-pressure orogenic

belt, east China and their relationship to lithospheric thinning. *Chem. Geol.* 222, 200–231. doi:10.1016/j.chemgeo.2005.07.006

Yu, P. P., Weinberg, R. F., Zheng, Y., and Finch, M. A. (2022). Multiple crustal melting pulses and Hf systematics in zircons. *Lithos* 410–411, 106583. doi:10.1016/j.lithos.2021.106583

Yuan, S., Li, H., Zhang, L. P., Li, C. Y., Liu, H. Y., Xue, Y. Y., et al. (2022). Geochemical and zircon Hf-O isotopic constraints on the origin of wulian A-type granite in Shandong peninsula, eastern China. *J. Earth Sci.* 33 (3), 609–622. doi:10.1007/s12583-021-1592-y

Zhai, M. G., Yang, J. H., Fan, H. R., Miao, L. C., and Li, Y. G. (2002). A large-scale cluster of gold deposits and metallogenesis in the eastern North China craton. *Int. Geol. Rev.* 44, 458–476. doi:10.2747/0020-6814.44.5.458

Zhang, H. F. (2012). Destruction of ancient lower crust through magma underplating beneath Jiaodong peninsula, North China craton: U–Pb and Hf isotopic evidence from granulite xenoliths. *Gondwana Res.* 21, 281–292. doi:10.1016/j.gr.2011.05.013

Zhang, L., Groves, D. I., Yang L QWang, G. W., Liu, X. D., Li, D. P., et al. (2020b). Relative roles of formation and preservation on gold endowment along the sanshandao gold belt in the Jiaodong gold province, China: Importance for province- to district-scale gold exploration. *Min. Depos.* 55, 325–344. doi:10.1007/s00126-019-00908-1

Zhang, L. P., Zhang, R. Q., Hu, Y. B., Liang, J. L., Ouyang, Z. X., He, J. J., et al. (2017b). the formation of the late cretaceous xishan Sn-W deposit, south China: Geochronological and geochemical perspectives. *Lithos* 290–291, 253–268. doi:10.1016/j.lithos.2017.08.013

Zhang, L., Weinberg, R. F., Yang, L. Q., Groves, D. I., Sai, S. X., Matchan, E., et al. (2020a). Mesozoic orogenic gold mineralization in the Jiaodong peninsula, China: A focused event at 120 ± 2 Ma during cooling of pregold granite intrusions. *Econ. Geol.* 115 (2), 415–441. doi:10.5382/econgeo.4716

Zhang, L., Yang, L. Q., Wang, Y., Weinberg R FAn Pand Chen B Y (2017a). Thermochronologic constrains on the processes of formation and exhumation of the Xinli orogenic gold deposit, Jiaodong Peninsula, eastern China. *Ore Geol. Rev.* 81, 140–153. doi:10.1016/j.oregeorev.2016.09.026

Zhao, G. T., Cao, Q. C., Wang, D. Z., and Li, H. M. (1997). Zircon U-Pb dating on the Laoshan granitoids and its significance. *J. Ocean Univ. Qingdao* 27, 382–388. (in Chinese with English abstract).

Zhu, R. X., Chen, L., Wu, F. Y., and Liu, J. L. (2011). Timing, scale and mechanism of the destruction of the North China Craton. *Sci. China Earth Sci.* 54, 789–797. doi:10.1007/s11430-011-4203-4

Zhu, R. X., Fan, H. R., Li, J. W., Meng, Q. R., Li, S. R., and Zeng, Q. D. (2015). Decratonic gold deposits. *Sci. China Earth Sci.* 58, 1523–1537. doi:10.1007/s11430-015-5139-x

Zhu, R. X., Yang, J. H., and Wu, F. Y. (2012b). Timing of destruction of the north China craton. *Lithos* 149, 51–60. doi:10.1016/j.lithos.2012.05.013

Zhu, X. Q., Wang, Z. G., Huang, Y., and Wang, H. L. (2004). REE content and distribution in apatite and its geological tracing significance. *Chin. Rare Earths* 25, 41. (in Chinese with English abstract).